Journal of Energy Storage 37 (2021) 102455

Contents lists available at ScienceDirect

Journal of Energy Storage

journal homepage: www.elsevier.com/locate/est

Emergence of rectangular shell shape in thermal energy storage applications: Fitting melted phase changing material in a fixed space

İsmail Gürkan Demirkıran, Erdal Cetkin *

Izmir Institute of Technology, Department of Mechanical Engineering, Urla, Izmir 35430, Turkey

ARTICLE INFO

Keywords:
Natural convection
Phase change material
Thermal energy storage
Design optimization
Shell and tube heat exchanger
S-curve

ABSTRACT

Here we document the effect of heat transfer fluid (HTF) tube position and shell shape on the melting time and sensible energy requirement for melting a phase change material (PCM) in a multitube latent heat thermal energy storage (LHTES) application. Tube location and shell shape are essential as the shape of the melted region, i.e. similar to the boundary layer, affects convective heat transfer performance. HTF tube total area is fixed in all cases to have the same amount of PCM. In order to eliminate the effect of heat transfer surface area variation, results of two- and four-tube configurations were compared within themselves. Liquid fraction, sensible enthalpy content, and latent/sensible enthalpy ratio relative to time were documented for two and four HTF configurations in various shell shape and tube locations. Results show that eccentric two tubes with rectangular shell decreases melting time and sensible energy requirement from 67 min to 32 min and from 161.8 kJ/kg to 136.3 kJ/kg for 72.3% liquid fraction, respectively, in comparison to the concentric tubes with the circular shell. When the number of HTF tubes increases to four, then the required melting time and sensible energy decrease 80% and 3.8%, respectively, for PCM to melt completely as the concentric tubes and circular shell is replaced with eccentric tubes and rectangular shell. Results of liquid fraction variation relative to time show that S-curve of melting becomes steeper if PCM distribution is such that the intersection of melted regions is delayed. Therefore, melted PCM regions could be packed into a shell that minimizes melting time and required sensible energy. Even rectangular shell shape increases the heat transfer surface (increased heat loss rate) because melting time has decreased greatly, total energy lost to the ambient from the surfaces of shell decreases. Eccentricity slows down the solidification process but due to increased heat loss rate from the surface, rectangular shell enables faster solidification than circular shell shape. There is a trade off in between solidification time and heat loss energy for rectangular channels which can be optimized by selecting proper insulation thickness. Overall, the results show that without any thermal conductivity enhancement (TCE) method, melting performance and latent heat storage capability can be significantly enhanced as decreasing the sensible heat storage by fitting the melted PCM regions into a fixed space for the applications where charging speed is lot faster than discharging.

1. Introduction

Pollution related to fossil fuels and an increase in their cost due to depletion created an urgent need for transition from conventional energy sources to renewables with enhanced energy-efficiency. One of the biggest problems related with them is the variation in the supplied energy due to the time-dependent characteristics of their energy harvesting methodology (wind, solar, currents, etc.). Therefore, feasible energy storage is required for renewable sources to take over the fossil sources. According to the International Energy Agency (IEA), 50% of the total energy consumption is in the form of heat, and 40% of CO_2 emission in the world is related to its generation. While nearly half of it is used for heating, cooling, and hot water need of residential buildings, the other half is used in industrial processes [1]. Therefore, solar thermal energy technologies can be prioritized to meet the world's heat energy needs. Besides, solar electricity generation plants can take part in curtailing the energy demand of conventional plants. In addition to the intermittent effects of nature, one more challenge for solar energy applications is not to be able to operate in the absence of solar radiation. Hence, thermal energy storage (TES) plays an essential role in the sustainability of solar energy. Moreover, the levelized cost of energy (LCOE) of concentrated solar power (CSP) plants has decreased greatly in recent years. Therefore, the LCOE of CSP plants with TES became 0.0185 $/kWh on average

* Corresponding author.
E-mail address: erdalcetkin@iyte.edu.tr (E. Cetkin).

https://doi.org/10.1016/j.est.2021.102455
Received 11 December 2020; Received in revised form 22 February 2021; Accepted 3 March 2021
Available online 15 March 2021
2352-152X/© 2021 Elsevier Ltd. All rights reserved.

Nomenclature

A	coefficient of momentum source term, kg/(m^3.s)
b	dummy constant
c_p	specific heat, kJ/(kg.K)
C	mushy zone constant, kg/(m^3.s)
f	liquid fraction
g	gravitational acceleration, m/s^2
h	total enthalpy, kJ/kg
k	thermal conductivity, W/(m.K)
L	latent heat capacity, kJ/kg
P	pressure, Pa
S_b	buoyancy source term, kg/(m^2.s^2)
S_h	energy source term, W/m^3
t	time, s
T	temperature, °C
u, v	velocity components, m/s
u	velocity vector
x, y	spatial coordinates, m

Greek symbols

μ	dynamic viscosity, kg/(m.s)
ρ	density, kg/m^3
β	thermal expansion coefficient, 1/K

Subscripts

l	latent
liquidius	liquification point
ref	reference condition
s	sensible
solidius	solidification point

in recent years, which is 40% lower than the price of 2010 [2]. Overall, TES plays an integral role to decrease the cost of renewables and making them more beneficial to use, i.e. solar plants can compete with conventional energy plants. In addition to solar energy, integration of TES also enhances performance of other renewables such as wind, geothermal, and their hybrid systems [3–5]. The energy in TES systems can be stored in the form of sensible, thermochemical and latent energy. Latent energy is advantageous to the others due to constant supply temperature and stored energy density. Therefore, phase change materials (PCMs) are widely being used for TES applications. Apart from TES, PCMs are also used for passive cooling of PV modules by achieving constant temperature in distinct PV cells [6]. Furthermore, PCM utilization can be found in many distinct fields such as thermal management of electronic devices [7], waste heat recovery [8], and HVAC [9] where latent heat storage is the primary aim.

Although PCM systems enable relatively high thermal energy storage capability, they come with the burden of relatively low thermal conductivity. Therefore, the literature focuses on active and passive heat transfer enhancement (HTE) techniques for energy storage with PCM applications. Active HTE techniques require additional energy input such as electrical, rotational [10], ultrasonic [11], etc. Passive HTE techniques can be categorized into three groups. First, thermal conductivity enhancement of PCM by embedding porous matrix or adding high thermal conductive nano-particles. Employment of porous foam decreases the solidification time more than the melting time. Even the porous foam enhances conductive heat transfer, it adversely affects the natural convection in large extents [12–14]. Uniform distribution of metallic or carbon-based nanoparticles both enhances the thermal conductivity of PCM composites and drops supercooling degree in remarkable magnitudes. However, nanoparticles can decrease latent heat capacity and increase the viscosity of PCM. Furthermore, they have the disadvantage of low cyclic stability due to agglomeration and sedimentation [15].

The second one is increasing overall conductance with extended surfaces. Inserting fin is one of the most commonly applied heat transfer enhancement techniques, and there exist several studies that investigate the fin shapes on heat transfer enhancement like the snowflake [16], tree-shaped [17], triangular [18], and so on. The general outcome is that fin length affects melting process more than fin thickness and number of fins. However, the fin has a bad effect on convection-driven melting, especially for horizontally-oriented LHTES systems due to suppress the upward movement of hot melted PCM [19]. Agyenim et al. [20] compared the melting processes of single-tube and multitube heat exchangers and revealed that enhancement in melting is not only by the increment in heat transfer surface area but also by the assignment of multiple natural convection-effectual melting zones in the PCM domain. Besides, Kousha et al. [21] and Esapour et al. [22] conducted experimental and numerical studies on the optimum number of multitubes, respectively. Parry et al. [23] numerically documented that even though the HTF-PCM contact surface area of the multi-tube case is 55% smaller than the longitudinal finned-tube case, the PCM melts 37% faster compared to the others.

The third method is to enhance heat transfer by varying the shape of shell tube and location of HTF tubes. In addition, arrangement of the HTF tube locations accelerates the melting process without additional construction costs and efforts where the literature on it is very limited. Luo et al. [24] documented the effect of HTF tube location on melting behavior of PCM by using the lattice-Boltzmann method. Their results revealed that since tubes do not inhibit the flow of melted PCM and they are well-distributed in the PCM domain, the melting rate of centrosymmetric alignment is better than the other competing cases. Dutta et al. [25] showed that when the HTF tube is moved along the downward direction, the charging time needed for the fully melted phase of PCM inside the heat exchanger is dramatically decreased. Eccentric tube design is also a promising approach due to being cost-effective as no additional material is required. Similar results in melting time are obtained in many other studies [26–28]. On the other side, it should be noted that the eccentric arrangement of the HTF tube causes discharging time to increase since solidification process is a conduction-dominant process, as reported in the study of Yazici et al. [29]. Zheng et al. [30] documented that although eccentricity decreases melting time significantly, it increases the solidification time greatly which also in agrees with Kadivar et al. [31]. In addition, the literature suggests hybrid methods of coupling eccentricity with porous foam insertion [32], nanoparticles [33], or fins [34] to enhance the conductive heat transfer rate during solidification. However, if the melting time is required to be lot shorter due to the characteristics of charging of energy in TES unit in comparison to the discharging time; then, eccentricity could be the sole method.

There are limited studies on the effect of shell and HTF tube shapes. For instance, Faghani et al. [35] employed elliptical cylinders for HTF tubes with the variable orientation of the cylinders to decrease melting time. Vogel et al. [36] documented that the effect of natural convection becomes dominant on heat transfer as the width of the enclosure increases and the height decreases for eutectic mixture of potassium nitrate and sodium nitrate (KNO_3—$NaNO_3$). Seddegh et al. [37] also documented the effect of orientation of the shell and tube heat exchangers on the melting time of PCM.

There are numerous PCMs, and finding the best fit for a specific application rely on application temperature. Applications such as solar-driven absorption cooling [38], solar collectors [39–42], parabolic dish absorbers [43], domestic thermal systems [44], heat transportation [45]

and district heating by industrial waste heat [46] require thermal energy storage at medium temperature range. Erythritol is one of the most promising materials for medium temperature applications due to its relatively high latent heat storage capability, i.e. almost two times greater than many competing PCMs [47], and studies on it are limited in the current literature.

Literature shows that the melting time of a TES system with erythritol as PCM can be decreased by altering the shape of the shell and positions of HTF tubes. However, it is not discussed why the competing designs were selected. The current study relies on design improvements on the shape of shell tube and positions of HTF tubes by considering the physics of the process, i.e., melted region characteristics based on conductive and convective heat transfer. Here, it is uncovered how the PCM can be melted without increasing temperature at the shell surface by locating HTF tubes further from them. In addition, how the S-curve of melting becomes steeper with design alterations based on the proposed methodology is discussed.

The study documents how melting time and heat losses can be decreased in a natural convection-driven melting (charging) process in a LHTES unit. The effects of geometric variations in HTF tube spacing, tube positions, and shell shape were examined to keep sensible heat enthalpy of melted PCM minimal and heat losses were reported for LHTES units with circular and rectangular shell designs. Furthermore, the proposed design improvements decreases melting time greatly in comparison to the solidification time. Therefore, proposed design methodology is suitable for the applications where charging the energy in the phase changing material (melting) is fast and discharging (solidification) is relatively slow.

2. Model description

2.1. Model

Fig. 1a illustrates the typical flow pattern of melted PCM inside a horizontally arranged shell-and-tube heat exchanger. The buoyancy force drives the melted PCM around the relatively hot tube to create circulation zones. The convection circulation enhances melting at the top and side regions, but it does not affect the bottom. Besides, the shell tube wall limits the natural convection dominancy when the melting interface reaches to the boundary. Therefore, two HTF tubes with outer shell tube have been chosen for the base design as in Fig. 1b. The diameters of the inner and outer tubes are 28.28 mm and 100 mm, respectively. Fig. 1c shows the numerical solution domain and mesh structure. The spacing between the two HTF tubes is equal to 20 mm. PCM (i.e., erythritol) is located inside the annulus region bounded by shell tube. Thermophysical properties of erythritol are listed in Table 1. Erythritol is selected because of its high latent energy storage capability, and it is not toxic nor corrosive.

Table 1
Thermophysical properties of PCM and insulation material [23].

Properties	Erythritol	Glass Wool
ρ_{ref} [kg/m^3]	1480	200
k [W/(m.K)]	0.733 at 20 °C, 0.326 at 140 °C (linear distribution)	0.04
C_p [kJ/(kg.K]	1.38 solid and 2.76 liquid (linear distribution)	2310
μ [kg/(m.s)]	2.7749 10–5 T2- 0.0231747 T + 4.844	–
L [kJ/kg]	339.8	–
$T_{solidius}$ [°C]	116.7	–
$T_{liquidius}$ [°C]	118.7	–
β [1/K]	0.001014	–

2.2. Governing equations

Transient melting process was simulated with the enthalpy-porosity technique [49]. Here it is assumed that the liquid phase of PCM is a Newtonian fluid, phase change occurs in isothermal condition ($T_{melting}$=$T_{solidius}$=$T_{liquidius}$ = 117.7 °C), and the effect of viscous dissipation is neglected. The maximum Rayleigh number is 5.97×10^6; therefore, flow is laminar during the melting process in all the simulations. With these simplifications are in mind, the conservation of mass, momentum along x-direction and y-direction become

$$\frac{\partial \rho}{\partial t} + \nabla(\rho \mathbf{u}) = 0 \tag{1}$$

$$\frac{\partial(\rho u)}{\partial t} + \nabla\cdot(\rho \boldsymbol{u} u) = \nabla\cdot(\mu \nabla \mathrm{u}) - \frac{\partial P}{\partial x} + Au \tag{2}$$

$$\frac{\partial(\rho v)}{\partial t} + \nabla\cdot(\rho \boldsymbol{u} v) = \nabla\cdot(\mu \nabla \mathrm{v}) - \frac{\partial P}{\partial y} + Av + S_b \tag{3}$$

where **u** is the velocity vector with u and v being velocity components along x and y directions, respectively. The buoyancy term is added in the y-momentum equation to assess the effects of buoyancy force, which arises from the temperature-based density variations of melted PCM, and it is expressed as below

$$S_b = \rho_{ref} g \beta (T - T_{ref}) \tag{4}$$

Here, ρ, μ, P, g, β, and T_{ref} are density, dynamic viscosity, pressure, acceleration of gravity, volumetric thermal expansion coefficient, and reference temperature, respectively. PCM is modeled as a quasi-porous medium. Therefore, porosity term 'A' is inserted into the conservation of momentum equations to satisfy the Carman-Kozeny relation. 'Au' and 'Av' terms are called 'momentum dissipation terms'. The function of these terms is to suppress the velocity of the PCM when it is in solid.

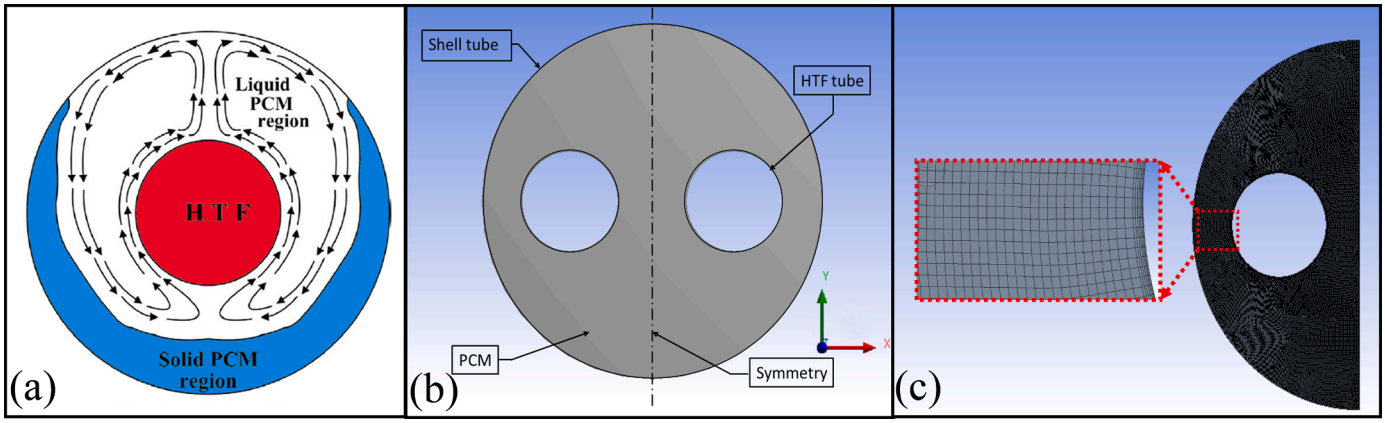

Fig. 1. (a) flow regime of liquid PCM inside a horizontal arranged shell-and-tube heat exchanger [48], (b) geometry of the base design, and (c) symmetric part of mesh structure for 2D numerical model.

Here, A equals

$$A = -C\frac{(1-f)^2}{f^3+b} \tag{5}$$

where C, and b are mushy zone constant, and a dummy constant to avoid division by zero, respectively. In simulations, $C = 10^5\,\mathrm{kg/(m^3 s)}$ and $b = 0.001$ were inserted. f, liquid fraction, represents the melted portion of PCM mass, and its value varies between 0 and 1, respectively. PCM domain is assumed to be fully melted and fully solidified when the liquid fraction of PCM is 0.99 and 0.01, respectively. The energy equation in enthalpy form is

$$\frac{\partial(\rho h)}{\partial t} + \nabla\cdot(\rho \boldsymbol{u} h) = \nabla\cdot(k\nabla T) \tag{6}$$

Here h and k are enthalpy and thermal conductivity, respectively. Enthalpy, h, represents the summation of sensible energy (h_s) and latent energy (h_l) contents where they are

$$h = h_s + h_l \tag{7}$$

$$h_s(T) = \int_{T_{ref}}^{T} c_p \mathrm{dT} \tag{8}$$

$$h_l = \begin{cases} 0 \mathrm{if T} < \mathrm{T}_{solidius} \\ \dfrac{T - T_{solidius}}{T_{liquidius} - T_{solidius}} L \mathrm{if T}_{solidius} < \mathrm{T} < \mathrm{T}_{liquidius} \\ L \mathrm{if T} > \mathrm{T}_{liquidius} \end{cases} \tag{9}$$

2.3. Initial and boundary conditions

Initial Condition

- The initial condition in the computational domain is:

$$t = 0, \mathrm{T(x, y)} = \mathrm{T}_i = T_m - 1^{\circ}C = 116.7^{\circ}C \tag{10}$$

Boundary Conditions

- Constant boundary temperature at the HTF tube walls:

$$T = T_{HTF} = 136.7^{\circ}C \mathrm{and} \Delta \mathrm{T} = \mathrm{T}_{HTF} - T_i = 20^{\circ}C \tag{11}$$

The PCM is initially subcooled 1 °C below to its melting temperature; therefore, the difference between the initial temperature of PCM and HTF tubes is 20 °C.

- Adiabatic boundary condition at the shell tube wall:

$$\left(\frac{\partial T}{\partial n}\right)_{shell\mathrm{tube}} = 0 \tag{12}$$

The outer shell wall was assumed to be adiabatic in accord with the literature because of negligible heat loss in LHTES units due to their well-insulated nature.

- Symmetry boundary condition at y-axis

$$u = 0, \frac{\partial}{\partial x}(u, v, T, P) = 0 \tag{13}$$

Across the symmetry line, velocity, temperature, and pressure gradients are equal to zero.

2.4. Model validation, mesh and time independency

The numerical studies were conducted by using a commercial computational fluid dynamics software, i.e. ANSYS 19.0 [50]. SIMPLE algorithm was used for pressure-velocity coupling. The convergence criteria are 10^{-5} for the conservation of mass and momentum equations and it is 10^{-10} for the conservation of energy equation.

The computer that simulations were carried out consists of 40 GB of RAM and two 12-core Intel® Xenon®E5–2630 CPUs. Each simulation in Fig. 2 requires around 4.7 million iterations that took almost five days (~120 h) with the specified computer. Therefore, the simulations were ceased when the fraction of melted substance is greater than 75%. Fig. 2 shows that phase change speed decreases considerably around 30th minute where conduction becomes dominant heat transfer mechanism. The quadrilateral mesh was used and as illustrated in Fig. 1c, the grid was intensified by inflation layers around the HTF tubes. In order to verify the grid independency of the numerical model, three different mesh sizes were compared with 6040, 11,547, and 17,933 nodes. Fig. 2 documents the effect of grid size in between 11,547 and 17,933 node cases is negligibly small for the present numerical model, so the mesh structure with the number of 11,547 nodes was adopted.

Time independency was also validated by comparing the liquid fraction outputs of the models whose time step size was chosen as 0.01 s, 0.05 s, 0.1 s, and 1 s. The results illustrated in Fig. 3 where they perfectly overlap, especially after the breakpoint of the liquid fraction graph. However, time step size of 1 s differs at the beginning of the process by 1.5%. Hence, time step size of 0.05 s was adopted for the following analysis of the study.

The numerical method was validated by the work of Parry et al. [23], in which the phase change process for Erythritol in a horizontally oriented single tube heat exchanger were investigated numerically and experimentally. The model was re-created by the same geometry (shell tube diameter of 152.4 mm, HTF tube diameter of 54 mm, HTF tube length of 1 m, insulation thickness of 100 mm) and same operating conditions (HTF inlet temperature of 140 °C, the initial temperature of 25 °C, HTF mass flow rate of 30 kg/min, heat transfer coefficient of $h_{air} = 10\,\mathrm{W/m^2K}$ at the insulation external surface) for validation. Heat transfer fluid is hot industrial oil which flows inside the HTF tube during the charging process, and PCM filled in the annulus region between the HTF tube and PCM container wall starts to melt. After the beginning of the melting process, the heated PCM container also triggers the melting of PCM from the outside. Fig. 4 shows that the PCM average temperature results of the current study and Parry et al. [23] are in agreement. In Fig. 4, PCM volume-averaged temperature increases gradually until the melting temperature, and then it passes to the long plateau stage. The authors describe the instant as the PCM is fully-melted, i.e. the time when the temperature exceeds the melting point of 117.7 °C. However,

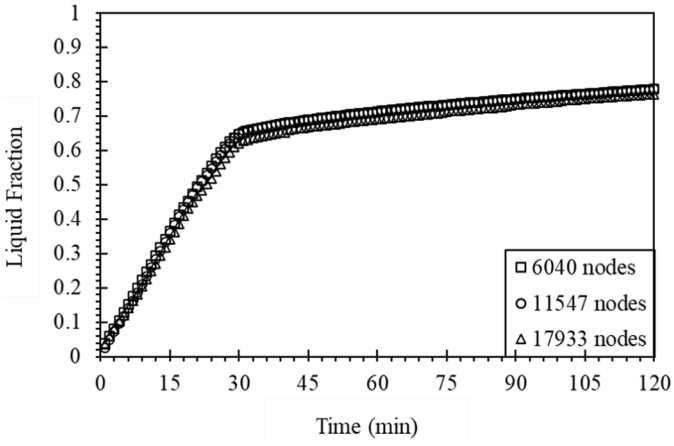

Fig. 2. Grid independency test.

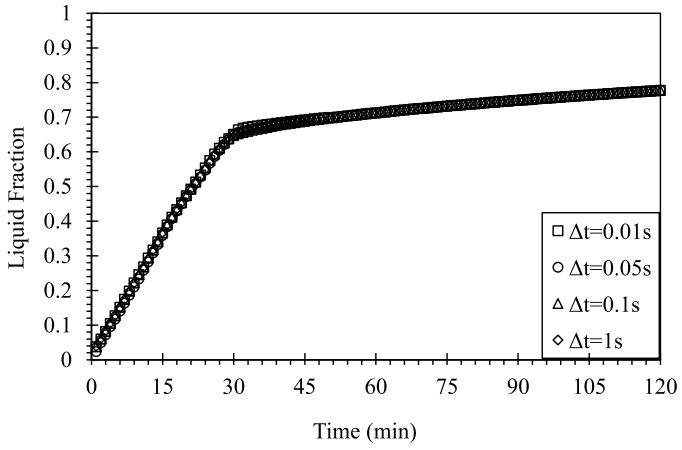

Fig. 3. Time independency test.

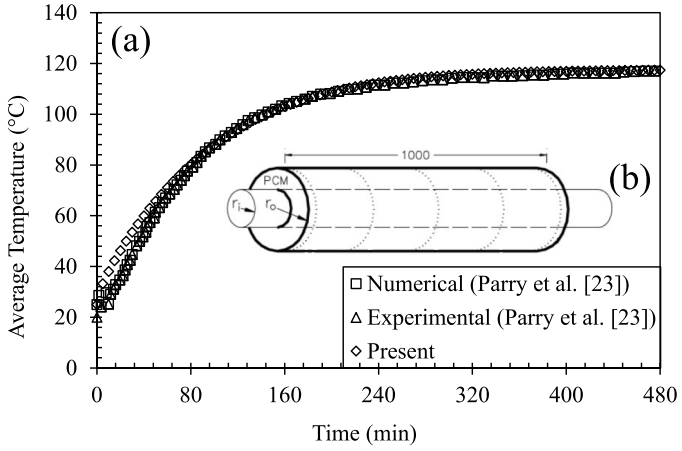

Fig. 4. (a)Comparison of the current study results with the results of Parry et al. [23], and (b)the schematic of shell-and-tube heat exchanger filled with PCM [51].

there may still be solid PCM, for example, possibly at the far bottom region of the PCM container as literature documents. Therefore, PCM volume-averaged temperature does not explicitly show whether the PCM is fully-melted or not. Hence, in the current study, liquid fraction and enthalpy content are preferred as parameters to track the melting ratio and to obtain stored heat in latent and sensible form distinctly, instead of volume-averaged temperature.

2.5. Latent/sensible enthalpy ratio(φ)

Many studies in the literature [51–55] document the comparison of melting models that neglect and do not neglect the natural convection terms in the governing equations. The general view is that if the natural convection effect included melting rate increases, the results become compatible with the experimental outputs. In addition, the error margin increases greatly if the numerical model does not include natural convection, i.e. pure conduction solution. Moreover, melting phase fronts and temperature distributions are greatly different from each other. On elucidating the strength of natural convection during the melting process, Rayleigh number indicates the ratio of buoyancy forces relative to viscous forces for the given boundary conditions and thermophysical properties of the PCM and defined as below:

$$Ra = \frac{g\beta\Delta T l_c^{\,3}}{\nu\alpha} \tag{14}$$

Ra number indicates that as the temperature difference ($\Delta T = T_{wall} - T_{melting}$) and length scale increases, the effect of natural convection would also become more pronounced especially in medium temperature applications such as in the current study. The maximum Rayleigh number is 5.97×10^6 in the current study with $\Delta T = T_{HTF} - T_{melting}$ and characteristic length is $l_c \sim D_{tube} = 28.28$ mm where the thermophysical properties of PCM and T_{HTF} evaluated at 136.7 °C.

The characteristic length, l_c, is also important for the natural convection effectiveness. In the study of Yanxia et al. [55], the PCM enclosure height is defined as the characteristic length in vertically oriented LHTES, and it is shown that the natural convection-driven melting process is enhanced by increasing Ra number associated with the height. Vogel et al. [54] states that there is a need for larger unconfined storage areas to make natural convection more pronounced in melting process, and adds that unless the PCM enclosure is designed with too high or too small aspect ratio, both height and width can be chosen as the characteristic length in vertically oriented heat exchangers since natural convection-driven melting of PCM grows at both vertical and horizontal directions. Moreover, in another study of Vogel et al. [36], a convective enhancement factor, $\varepsilon(f_l) = \frac{Q(f_l)_{convection}}{Q(f_l)_{conduction}}$, which is the heat flux ratio of the natural convection relative to the model accounts only pure conduction heat transfer. The enhancement factor is a measure of natural convection impact on the melting process, and the results show that with increasing Ra_{Width}, the strength of natural convection becomes more effective.

As for horizontally oriented LHTES units, in order to constitute Ra number, the hydraulic diameter of the HTF tube or $l_c = R_{shell} - R_{tube}$ which corresponds to the PCM layer thickness are used for the characteristic length in single-tube heat exchangers. With multiple tube utilization, the characteristic length is updated to $l_c = R_{shell} - nR_{tube}$ (n: number of HTF tubes) [21,23,56,57]. Since the annular region enlarges by applying eccentricity to the HTF tube $l_c = R_{shell} - d_{ecc}$ was proposed in Dutta et al. where d_{ecc} is the distance between shell center to eccentric tube's center [25]. However, these characteristic lengths used in literature may not satisfy the assessment of natural convection in the melting process since depending on the melted region thickness heat transfer can be pure conduction as its effect is dominant at first, natural convection with internal flow characteristics or external flow characteristics. Therefore, defining a Ra number that is dependent on geometrical length scales may not match with the real physical characteristics. Therefore, the ratio of latent enthalpy over sensible enthalpy, φ, is defined to uncover how the design alterations enhance thermal energy storage performance where φ is

$$\varphi = \frac{h_l}{h_s} = \frac{fL}{\int c_p dT} \tag{15}$$

The minimization of sensible heat storage is also essential which minimizes heat loss from TES to the ambient where solid PCM behaves similar to an insulation material until it melts entirely. In the current study, since no TCE methods was employed such as nanoparticle or porous foam addition, melting rates accelerate due to natural convection enhancement related with arrangement and geometry.

3. Two concentric tubes in a circular shell

Consider two HTF tubes inserted in a circular shell as shown in Fig. 1b. Fig. 5a shows the development of liquid fraction contours for five distinct times. The contours represent how the PCM melts almost from 0 vol fraction to the time when melting speed decreases greatly. First, the main heat transfer mechanism is conduction and melted region thickness grows gradually in both x- and y-directions, i.e. as can be seen in Fig. 5a at 2nd minute. At that time, multiple circulations start to show up near the upper surface of the HTF tubes as shown in streamline contour, Fig. 5b. Then natural convection dominates melting due to

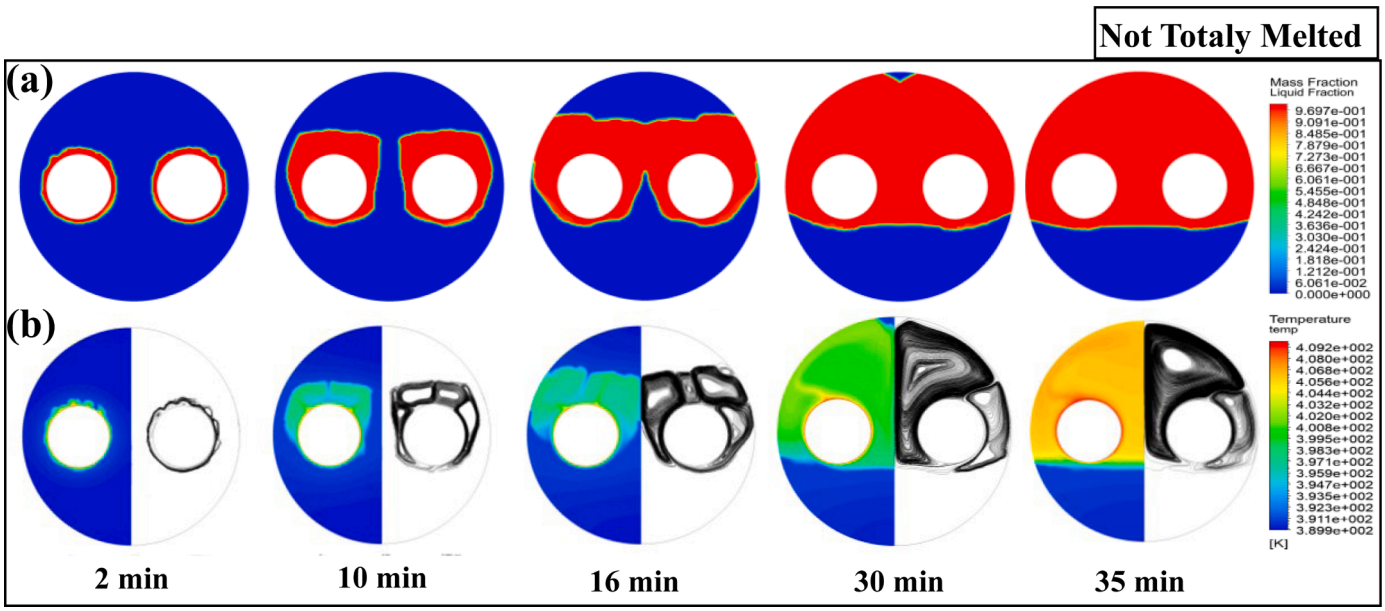

Fig. 5. Evolution of (a)liquid fraction and (b)temperature (at left side) and streamline (at right side) for two-tube *'Concentric Tubes/Circular Shell'* case.

increased buoyancy force which is driven by the density field and gravitational acceleration. Circulations combine to large ones, and the melting region grows toward lateral and upward directions as depicted in Fig. 5, 10th min. The melted region becomes asymmetric as the convection mechanism dominates, i.e. thicker melted region above the HTF tube as can be seen in Fig. 5a 10th minute. The melted regions around HTF tubes do not affect each other until the time when they intersect at 16th minute. Then, melting speed decreases as can be seen in Fig. 5a. This implies transferred energy is stored as sensible enthalpy rather than latent one. Also, temperature contours were seen in Fig. 5b prove that overheating begins to come into sight after the merging of melted regions. However, with the intersection of melted PCM interface of each HTF tubes, the strength of convection circulations weakens which decelerates the melting speed. Last but not least, as the region above HTF tubes melts entirely, the melting process is dominated by the conduction which occurs below the HTF tubes. Temperature contour and streamline for 35 min clearly show that natural convection only exists at the top region where PCM is totally in the liquid phase and it is exposed to overheating. In order to uncover specific transition times, variations of liquid fraction, latent/sensible enthalpy ratio, and sensible enthalpy based on time are shown in Fig. 6.

Fig. 6 also shows the contour of liquid and solid substance distribution where they are represented with red and blue colors, respectively. Fig. 6a shows 65% of the substance melts in 30 min, and melting from 65% to 72.3% takes 37 more minutes. The characteristics of liquid fraction is an S-curve. Fig. 6a also shows that the ratio of the latent/sensible enthalpy decreases as the heat transfer mechanism becomes pure conduction again at the 30th minute, and it reaches the maximum level, $\varphi = 153\%$. After that time, the melting rate decreases dramatically, and the sensible enthalpy rises as can be seen in Fig. 6b. Fig. 6b also shows that the amount of sensible heat begins to increase greatly when two melted regions around HTF tubes intersect, and it ramps up when no solid PCM remains at the top region. Therefore, relocating the PCM regions from the bottom section of HTF tubes where it melts slowly to the upper part may increase the phase change speed. Here, the melting front seen in Fig. 6a suggests that eccentric HTF tubes as well as a shell with a flat-edged bottom surface may minimize sensible heat storage in addition to decrease melting time. The S-curve of melting is aimed to be in a steeper trend to minimize melting time as discussed in Ref. [58].

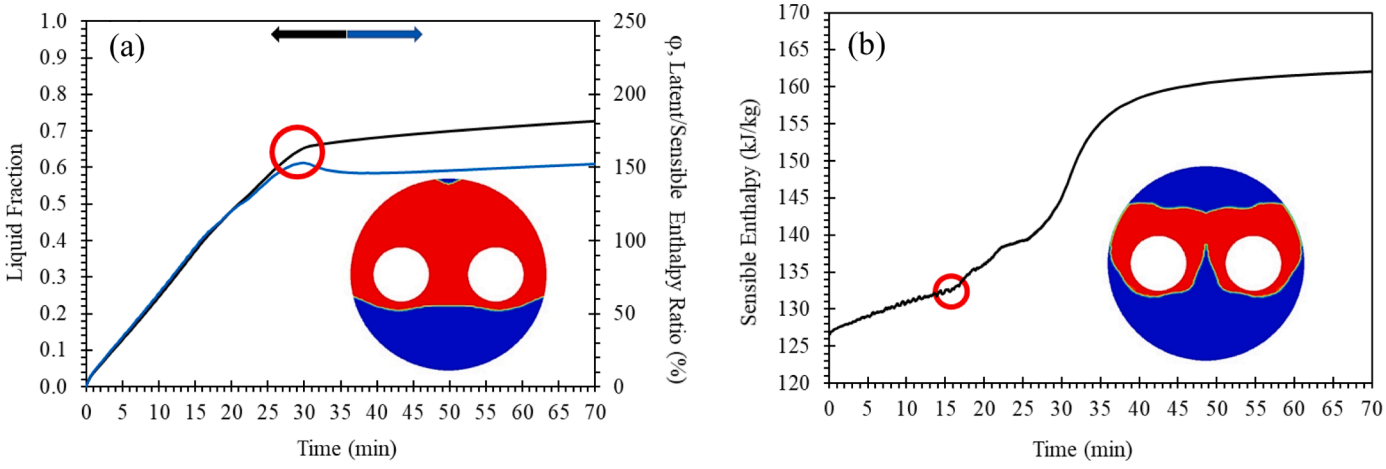

Fig. 6. Transient variation of (a) liquid fraction (top line) and latent/sensible enthalpy ratio φ (bottom line), and (b) sensible enthalpy of LHTES system for two tube *'Concentric Tubes/Circular Shell'* case. (For interpretation of the references to color in this figure legend, the reader is referred to the web version of this article.)

4. Two eccentric tubes in a rectangular shell

The results of Fig. 6 document that the melting process slows down and the majority of the stored energy becomes the sensible one after the melted regions intersect. Liquid PCM rises to the top and circulates as it gets further from the heat source. Therefore, the melting front expands also in the horizontal direction. The confinement of the convection circulations is stemmed from insufficient tube spacing and circular shell shape that is inappropriate to the growth of melting front. Eccentric HTF tube helps to avoid conduction-dominant regions such as the condition of the base case at the time of 35th min in Fig. 5. However, with increasing the spacing between HTF tubes, the eccentricity that can be applied to two HTF tubes would not be enough totally to avoid solid PCM domain located at the bottom and melts via conduction. Because the width of a circular-shaped shell decreases along the y-axis. That makes a shell with a flat-edged bottom surface a better candidate to apply eccentricity. Therefore, it can be concluded that alteration in shell shape may yield a melting process where the melting speed would not decrease as the intersection of melted fronts is avoided. The results also show that before the intersection time, melting in tubes does not affect each other due to their symmetrical nature. The melting front grows through not only upward direction but also lateral direction as happened in the base case, and more PCM can be melted between the tube spacing region if melting fronts progress without merging. Thus, the intersection of melted fronts is undesired. The shell design can be improved with the displacement of melted PCM regions around HTF tubes, i.e. packing melted regions rather than packing HTF tubes in a shell. Fig. 6b shows that the melted regions become almost a rectangular region where the tubes are located near the bottom of the rectangle. Please note that the volume of the PCM material and HTF tubes are kept constant. Therefore, the tube spacing raises from 20 mm to 30 mm. The length scale of the shell is 116.56 mm × 67.38 mm. The distance from the bottom of the shell to the inner tubes is 5 mm.

Fig. 7a shows the growth of liquid fraction of two-tube *'Eccentric Tubes/Rectangular Shell'* case. The melted zones of each tube grow independently until the time of 37 min. Note that this time is longer than the previous design where it is 16th minute. This is because the volume is constant and the distance in between the tubes is greater. Therefore, while 35% solid melted in the previous case until two melted regions intersect, it is 85% in the rectangular case. In addition, the instant that melted PCM is exposed to overheating is delayed. The comparison of temperature contours for 41st and 46th min in Fig. 7b clearly explains the effects of overheating after the intersection of the melted regions. Fig. 7 shows how PCM melts in the rectangular shell in time. The figure suggests moving the tubes a little bit more down. However, for the sake of simplicity, it is not going to be considered.

After the intersection of melted fronts, sensible enthalpy starts to rise in a steeper trend, as happened in the base case as shown in Fig. 6b. Fig. 8a also documents that the latent enthalpy ratio decreases as the region above tubes are melted similarly. φ reaches its maximum values of 216% at the 41st minute. However, Fig. 8a also shows more than 92% of PCM is melted, unlike 65% of the previous case. Fig. 8b also shows the sudden increase trend in sensible heat is postponed greatly with shell design alteration. This accelerates the melting rate greatly, but there is still solid PCM. The rectangular design satisfies 92% of PCM to melt quickly by natural convection in the first 41 min until there is no considerable temperature change in the melted PCM as shown in the contours of Fig. 7b. However, melting the rest of PCM requires additional 26 min.

Fig. 9 uncovers the advancement of rectangular shell design relative to the base design. Fig. 9a shows the amount of sensible and latent enthalpies for the base design, *'Concentric Tubes/Circular Shell'*, of Fig. 5 and the improved design, *'Eccentric Tubes/Rectangular Shell'*, of Fig. 7. At the 37th minute, the rectangular shell design, Fig. 7, stored 25% greater heat in latent form and 12% less heat in the sensible form in comparison to the circular shell design, Fig. 5. However, the rectangular stored 10% more heat in total. This proves that the storage unit should be designed, focusing on the latent heat capability. As for 67th minute values, the difference between latent heat storage of the rectangular, Fig. 7, and circular, Fig. 5, designs increase from 25% to 38%, and sensible enthalpies become the same. Fig. 9b shows that the S-curve of melting becomes steeper with the improvements on the shell design. For the time (67th min) in which improved rectangular design reached fully melted condition, increasing of tube spacing, the eccentric arrangement of the HTF tubes, and change of circular shell to a rectangular one for the sake of sufficient eccentricity caused a 38% enhancement in melting with respect to the base design. Fig. 9c shows the sensible enthalpy storage in designs of Figs. 5 and 7 are same the until 16th minute. Then, sensible heat storage increases rapidly in the design of Fig. 5 because the melted regions intersect and the rate of increase diminishes. Whereas the melted regions intersect at the 37th minute for the design of Fig. 7, and sensible heat storage increases rapidly and becomes greater than the one for the design in Fig. 5. However, Fig. 9a shows this increase in sensible heat relatively small in comparison to the total heat storage and increment in the latent heat storage.

5. Four concentric tubes in a circular shell

It is commonly confirmed that increasing the heat transfer area by the utilization of more tubes will lead to progress in the melting process when the volume is fixed (as heat transfer surface area/volume ratio increases). Note that the total heat transfer length of the two-tube design is 178 mm with $D_{tube} = 28.28$ mm. On the other hand, the total heat transfer length of four-tube designs is 251 mm with $D_{tube} = 20$ mm. However, the volume of PCM and tubes are the same as in the previous sections.

Consider four HTF tubes concentrically inserted in a circular shell as shown in Fig. 10. The HTF tubes were located considering the tube

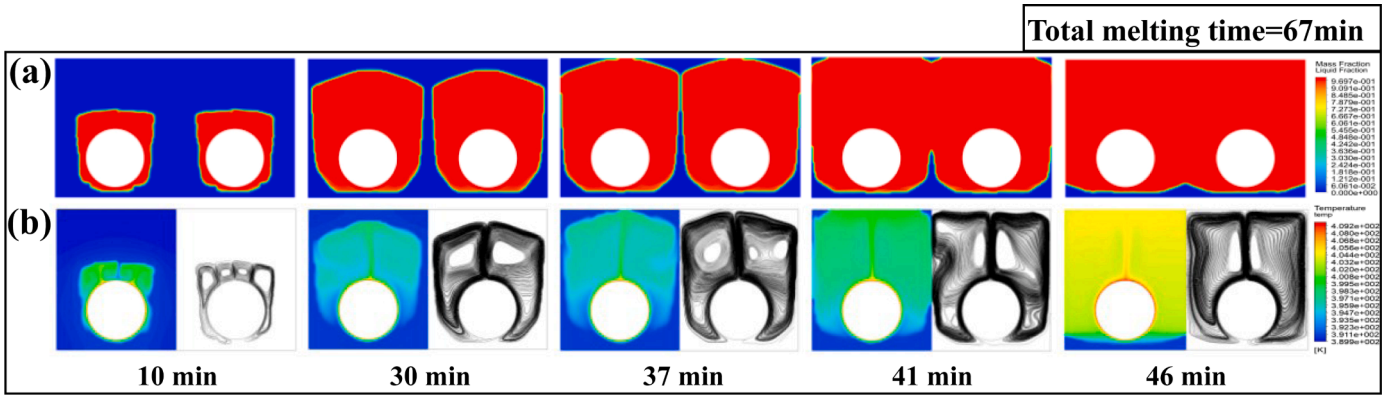

Fig. 7. Evolution of (a)liquid fraction and (b)temperature (at left side) and streamline (at right side) for two-tube *'Eccentric Tubes/Rectangular Shell'* case.

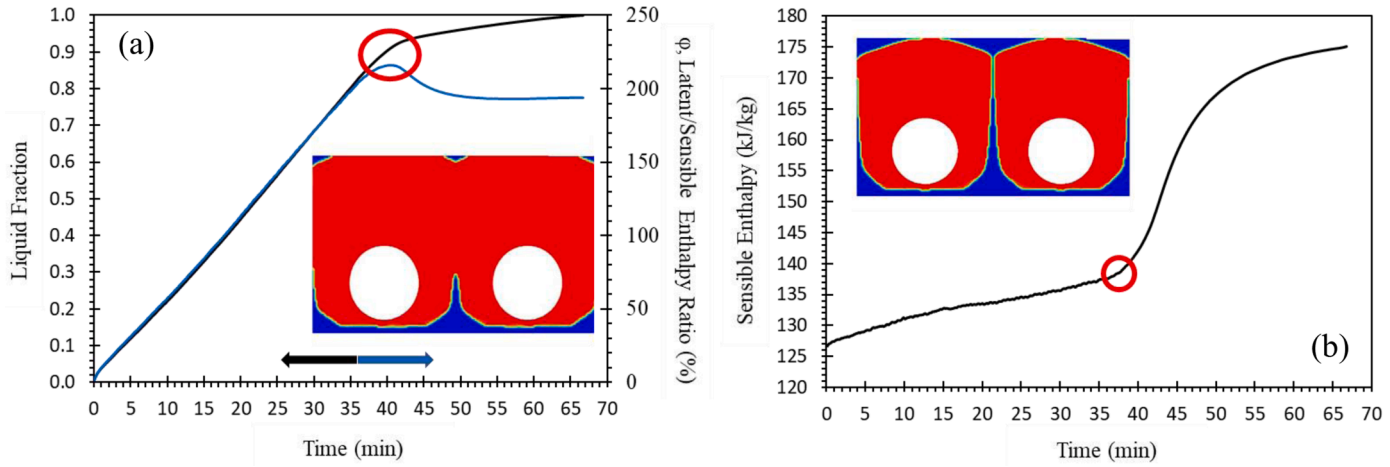

Fig. 8. Transient variation of (a) liquid fraction (top line) and latent/sensible enthalpy ratio φ (bottom line), and (b) sensible enthalpy of LHTES system for two- tube *'Eccentric Tubes/Rectangular Shell'* case with rectangular shell. (For interpretation of the references to color in this figure legend, the reader is referred to the web version of this article.)

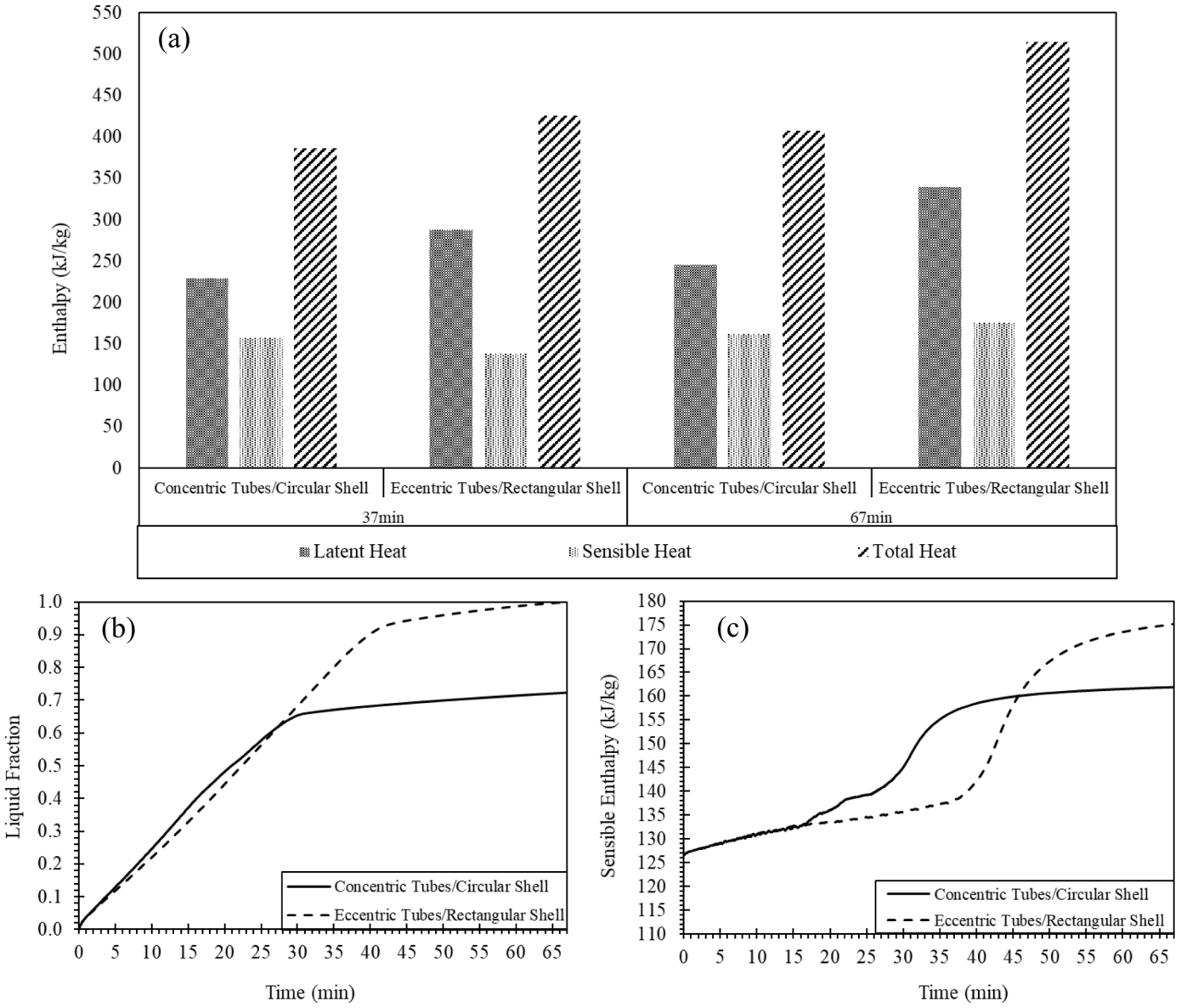

Fig. 9. Evolution of (a)liquid fraction and (b)temperature (at left side) and streamline (at right side) for four-tube *'Concentric Tubes/Circular Shell'* case.

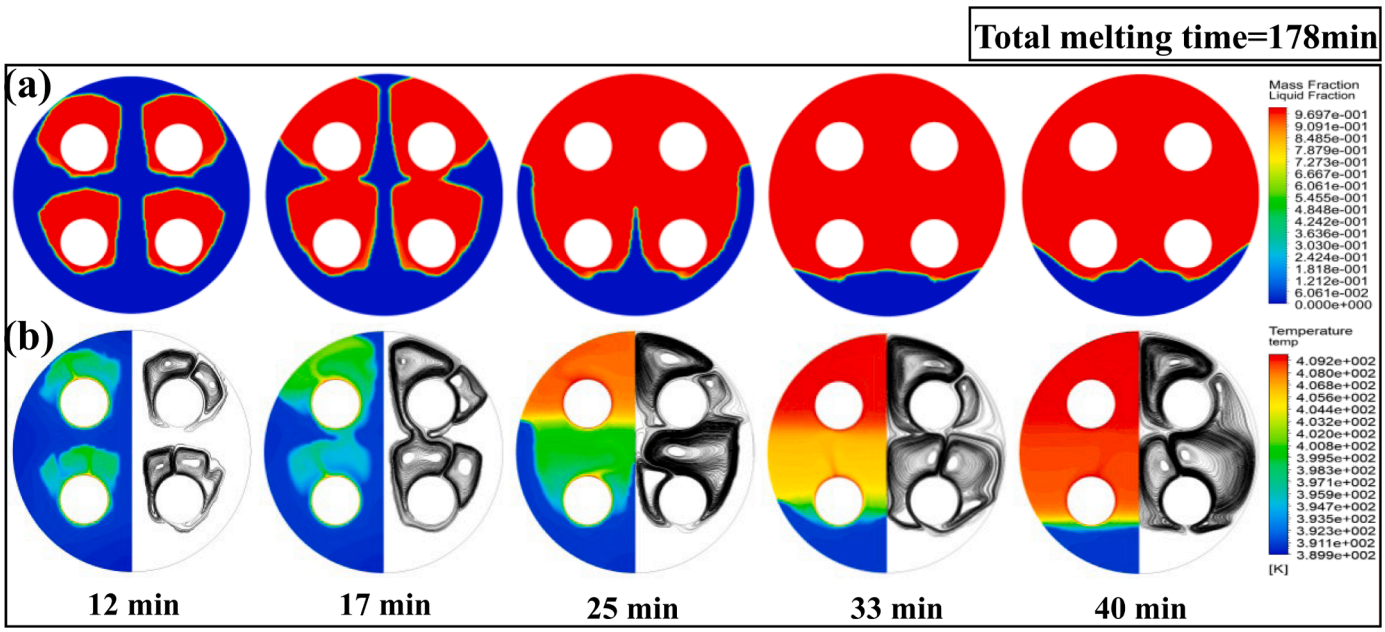

Fig. 10. Comparison of two-tube *'Concentric Tubes/Circular Shell'* and *'Eccentric Tubes/Rectangular Shell'* cases for (a) total enthalpy, (b) liquid fraction, and (c) sensible enthalpy.

spacing among each other to be equal to 20 mm.

An increase in melting rate is expected in four tube cases due to the increase in the heat transfer surface area. However, if the design is concentric, the bottom of the shell is far away from the surface of the tubes again. This yields conduction to be dominant in the melting of the bottom region as in the design of Fig. 5. Fig. 10a shows that growth of the melted region is limited by the outer tube at the 12th minute of the melting process. And at the 17th minute, the melted liquid of the upper and lower tubes touch with each other. Temperature contour of 17th min shows that while the melted region around the lower tube is not exposed to overheating, the temperature of melted PCM at the top region of the upper tube is higher than the rest of the melted domain. That is because melting is restricted by the upper edge of the shell tube. Furthermore, streamline contours of 12th and 17th mins reveal that circulations of upper and lower melting regions are different due to the shell-caused restriction. Solid PCM amount decreases at the region upside the HTF tubes, melted PCM temperature increases as can be clearly seen in temperature contours of Fig. 10b for the 25th min. After the 33rd minute, the melting by natural convection diminishes, and the process transits to the plateau stage as shown in Fig. 11a. The latent/sensible enthalpy ratio, φ, gains its highest value of 190% at this time. In the first 33 min, 83% of the PCM melts, but the rest requires additional 145 min. In addition, Fig. 11b shows that sensible enthalpy begins to increase rapidly after the 17th minute (i.e., when the melting regions intersect). The reason why sensible enthalpy increase transits to the plateau stage after 40th min is that sensible heat content of the PCM reaches close to its upper limit under the applied temperature boundary condition, which can be seen in the temperature contour of 40th min.

Please also note that when *'Eccentric Tubes/Rectangular Shell'* two-tube design of Fig. 7 and *'Concentric tubes/Circular shell'* four-tube design of Fig. 10 are compared, whose time needed for the fully-melted condition are 67 and 178 min, respectively. The two-tube design of Fig. 7 caused a 62% shorter melting time even if its heat transfer surface area is less than the four-tube design of Fig. 10. This situation proves that suitable HTF tube position, the eccentricity of the tubes, and alteration in shell shape is an effective approach.

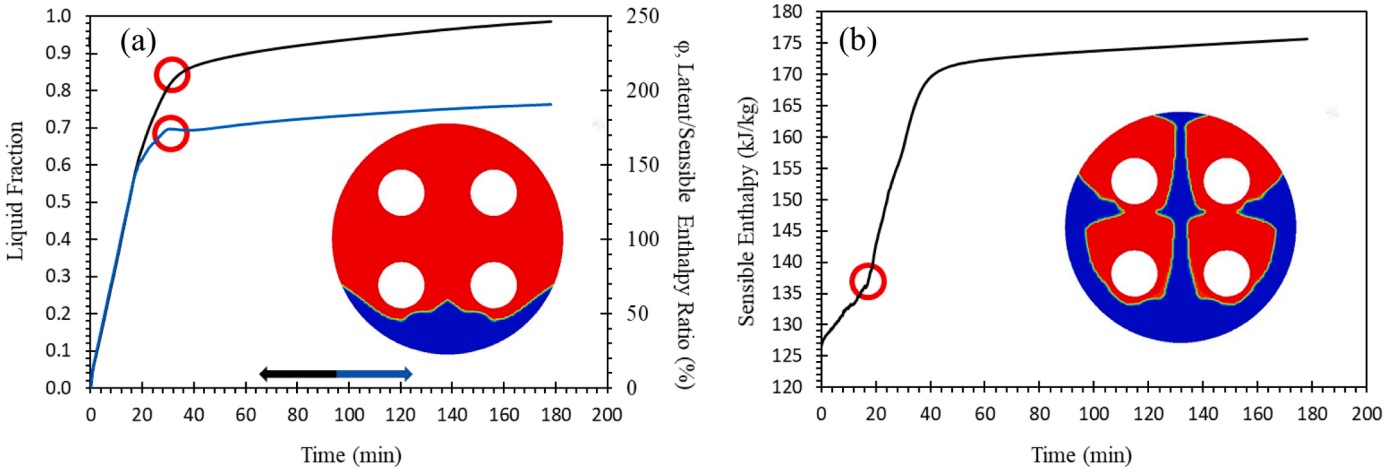

Fig. 11. Transient variation of (a) liquid fraction (top line) and latent/sensible enthalpy ratio (bottom line), and (b) sensible enthalpy of LHTES system for four-tube *'Concentric Tubes/Circular Shell'* case. (For interpretation of the references to color in this figure legend, the reader is referred to the web version of this article.)

6. Four eccentric tubes in a circular shell

Consider HTF tubes in Fig. 10 moved down to enhance melting rate as shown in Fig. 12, i.e., tubes were shifted 11 mm downward without changing the arrangement. The tube spacing remained the same, so the length of the four-tube design occupies on the horizontal direction is around 16 mm shorter than the two-tube circular shell design, and so it is suitable to move down even more.

Fig. 12 shows that melted regions located below the tubes touch to the shell at the 3rd minute. The melted PCM layer of each tube grows individually until they intersect at the 19th minute. On the contrary to previous cases, sensible enthalpy begins to increase rapidly when circulation zones of all tubes melt solid PCM located in the center of the shell at 26th minute, as depicted in Fig. 13b. After 26th min, the temperature contours support the increase in sensible enthalpy of PCM, and streamlines of upper and lower melted regions intersected at the left and right sides. Here, the time of the melting process to transit to the plateau stage is the 31st minute, at which φ reaches the top point with the value of 213% as can be seen in Fig. 13a. The liquid fraction contours of Fig. 12 eccentric four-tube design show that removing the solid region at the bottom from the shell may increase the melting rate as in two tube cases.

7. Four eccentric tubes in a rectangular shell

Here the melted regions are packed into the fixed space as discussed in the two tube case. However, in order to have a manufacturable design, the shell is decided to be rectangular. Likewise, in previous sections, the volume of the PCM and tubes are fixed. Center to center distance between the HTF tubes is 24 mm, and the side tubes are located 12 mm further from the vertical wall of the shell. The length scale of the shell is 175.6 mm × 44.72 mm. The previous cases documented that the region below the tubes melts slowly due to the dominant heat transfer mechanism is conduction. Therefore, the distance between the bottom edge of the shell and the inner tubes was reduced to 2 mm.

Fig. 14a shows how the melting occurs in four tube case with a rectangular shell relative to the time. At the 3rd minute, the melted region below the tube touches the shell and begins to expand in the horizontal direction. By the 25th minute, the melted regions merge. 91% of PCM melted at the 27th minute, and the rest required 8 more additional minutes as can be seen in Fig. 15a. This result shows the rectangular shell design is superior to the previous ones. In addition, Fig. 15b confirms that the sensible heat begins to increase rapidly as the melted regions touch and their top intersects with the top of the shell. Likewise, the results of the rectangular design of Fig. 7, overheating occurs only at the last minutes of the melting process. Also, the streamline of 34th min reveals that circulations around the HTF tubes combine at the top region when PCM reaches almost fully melted. The maximum point of the latent/sensible enthalpy ratio line corresponds to 220%, and this value is the highest one in comparison to previous cases'.

In order to compare the effect of the HTF tubes' positions, tube spacing, and shell design, the results of the four-tube designs are compared in Fig. 16. Fig. 16a shows that melting time decreases and S-curve melting becomes steeper as the tubes are located in an eccentric fashion and even more with rectangular shell shape. Please note that the S-curve of melting is the same until the breakpoints where there is almost no more solid PCM to melt at the top regions for each case. Then, the trend changes.

Fig. 16b and 16c show that sensible enthalpy becomes the smallest with the rectangular shell design while it is also the first one that reaches 100% liquid fraction. This shows that packing melted regions into a shell is a valid approach that is also easier to conduct in comparison to exhaustive search. The figures also show that the *'Eccentric Tubes/Circular Shell'* design yields an increase in both sensible and total energy until PCM melts entirely in comparison to the concentric one, i.e., 1.1% and 0.7% increase in the sensible and total enthalpies, respectively. This relatively small increase can be explained by the enhanced natural convection in between the region near the tubes. Thermal conductance increases as the length scale of the melted region increases. Overall, Fig. 16 documents that the tubes placed in a rectangular shell design called *'Eccentric Tubes/Rectangular Shell'* yields 80% and 35% decrease in melting time according to *'Concentric Tubes/Circular Shell'* design of Fig. 10 and *'Eccentric Tubes/Circular Shell'* design of Fig. 12, respectively.

8. The effect of shell shape and eccentricity on heat loss and solidification

Rectangular shells with eccentric HTF tube locations decreases the melting time and sensible heat storage greatly. The effect of shell shape on solidification and heat loss are also essential when the cycle of melting and solidification is considered. Therefore, four eccentric tubes

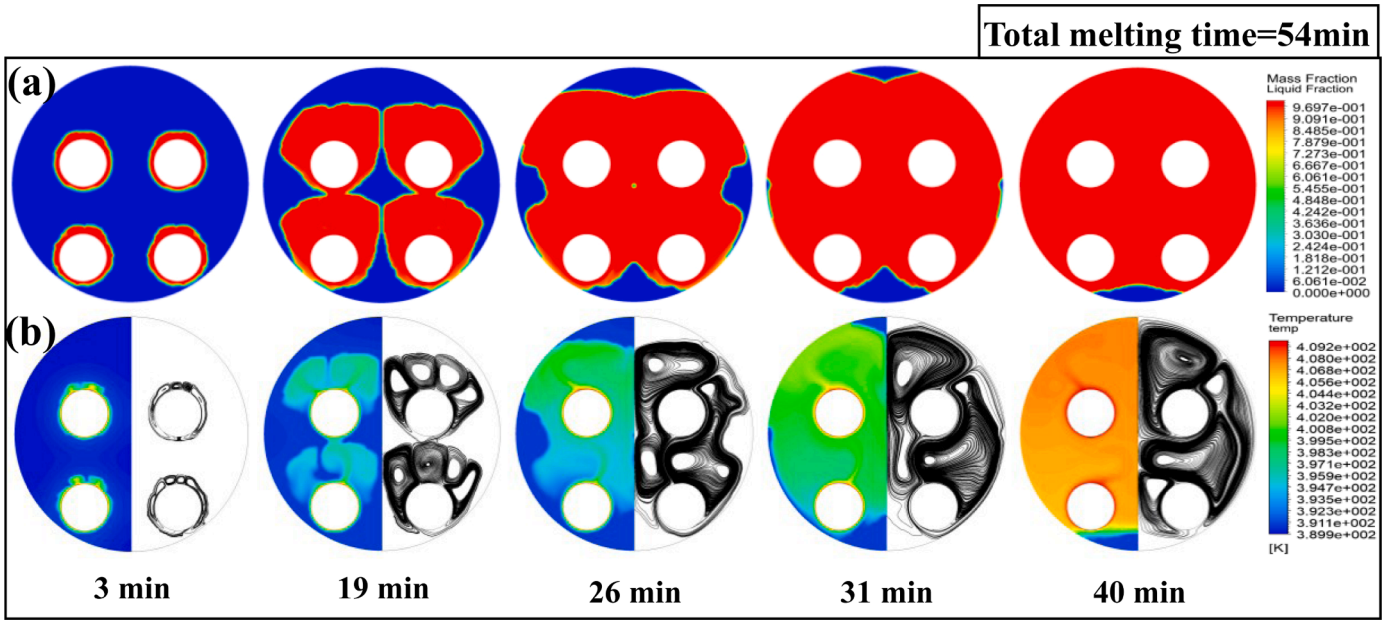

Fig. 12. Evolution of (a)liquid fraction and (b)temperature (at left side) and streamline (at right side) for four-tube *'Eccentric Tubes/Circular Shell'* case.

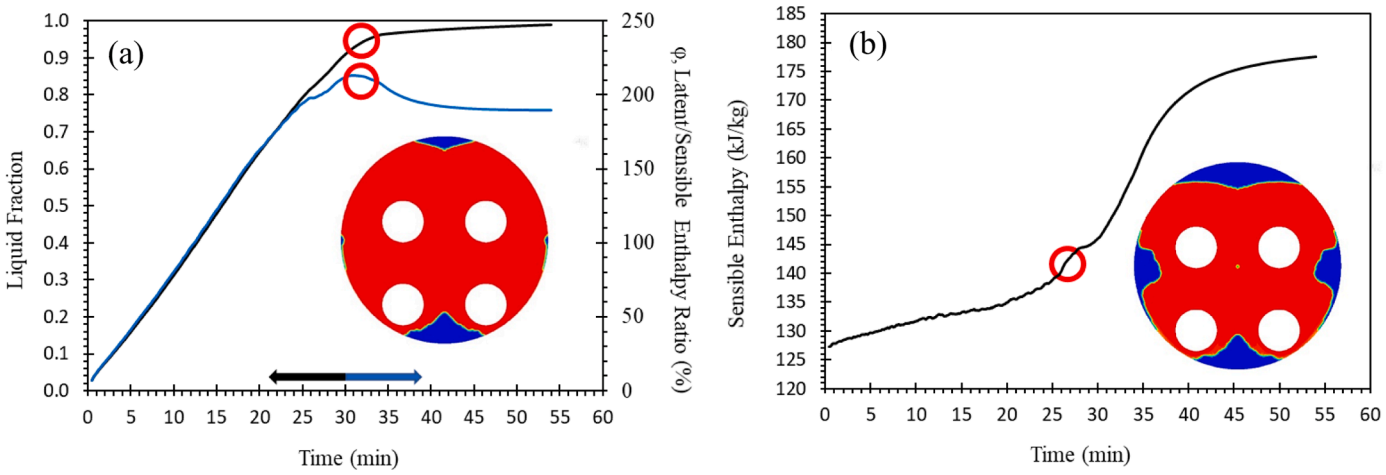

Fig. 13. Transient variation of (a) liquid fraction (top line) and latent/sensible enthalpy ratio (bottom line), and (b) sensible enthalpy of LHTES system for four-tube *'Eccentric Tubes/Circular Shell'* case. (For interpretation of the references to color in this figure legend, the reader is referred to the web version of this article.)

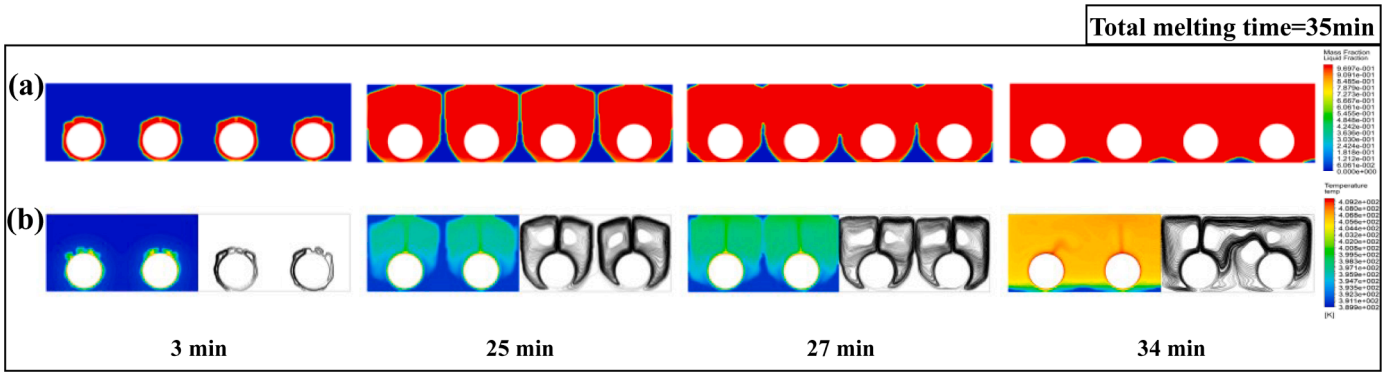

Fig. 14. Evolution of (a)liquid fraction and (b)temperature (at left side) and streamline (at right side) for four-tube *'Eccentric Tubes/Rectangular Shell'* case.

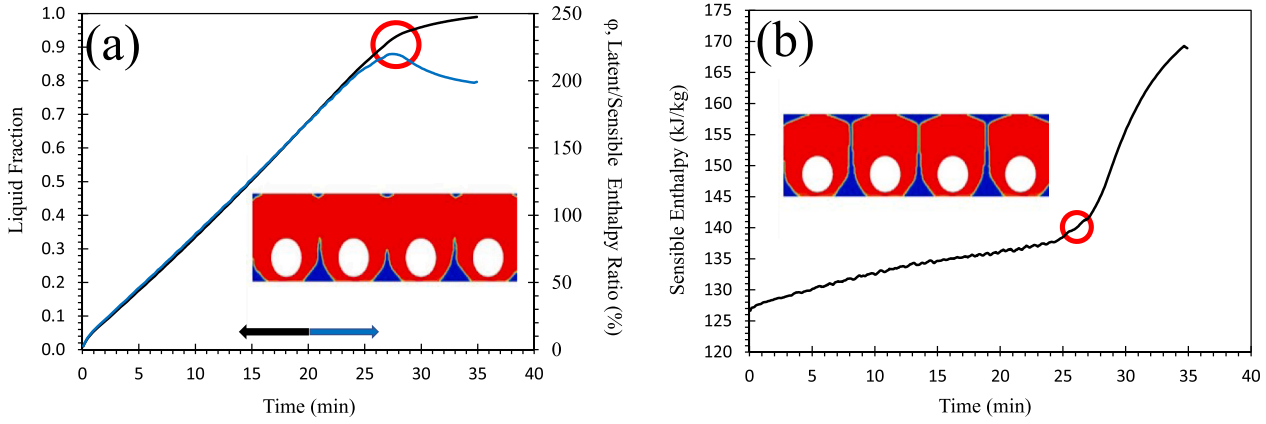

Fig. 15. Transient variation of (a) liquid fraction (top line) and latent/sensible enthalpy ratio (bottom line), and (b) sensible enthalpy of LHTES system for four-tube *'Eccentric Tubes/Rectangular Shell'* case. (For interpretation of the references to color in this figure legend, the reader is referred to the web version of this article.)

in a circular shell and in a rectangular shell designs were simulated with non-adiabatic boundary conditions for both melting and solidification processes.

As applied in the study of Parry et al. [23]., an insulation thickness of 100 mm was defined in the circular design, and glass wool was used as insulation material. Its thermophysical properties can be seen in Table 1. Outer surface of the insulation is a convection boundary with $h_{air} = 10\ W/m^2K$ and $T_{ambient} = 25\ °C$. Besides, the initial temperature of the insulation thickness was set to 116.7 °C so that the whole domain is initially 1 °C subcooled below PCM melting temperature. To establish a coherent comparison of the heat loss effect among different shell designs, the volume of insulation material is fixed for both designs. Hence, insulation thickness defined in the four-tube 'Eccentric Tubes/Rectangular Shell' case corresponds to 39 mm. Insulation external wall perimeters are 628 mm and 756 mm for circular and rectangular shell designs, respectively.

After the PCM is completely melted, the solidification process begins with a constant temperature 19 °C below the PCM melting temperature

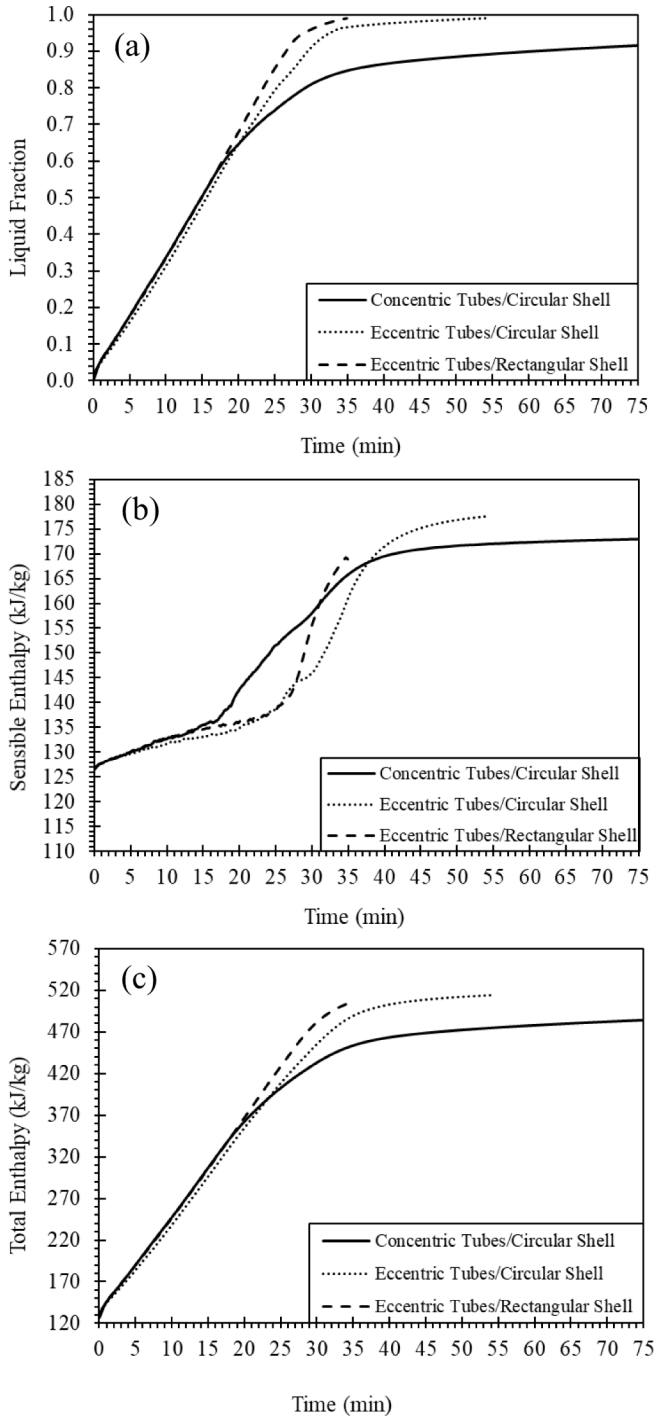

Fig. 16. Comparison of four-tube *'Concentric Tubes/Circular Shell'*, *'Eccentric Tubes/Circular Shell'*, and *'Eccentric Tubes/Rectangular Shell'* cases for (a) liquid fraction, (b) sensible enthalpy and (c) total enthalpy.

at the HTF tubes. The solidification process was terminated when there is no liquid PCM inside the shell.

The evolution of melting process in non-adiabatic conditions is almost the same as the adiabatic one. Only difference is the time delay due to heat losses. The charging process takes 61.5 min which is 7.5 min more than the previous adiabatic case. Melting initially occurs around the HTF tubes and develops at the top region due to upward movement of melted PCM as can be seen in Fig. 17a. At the last stage of the melting process, only solid PCM exists at the bottom of the LHTES unit, and melted PCM is exposed to overheating during the time required to melt

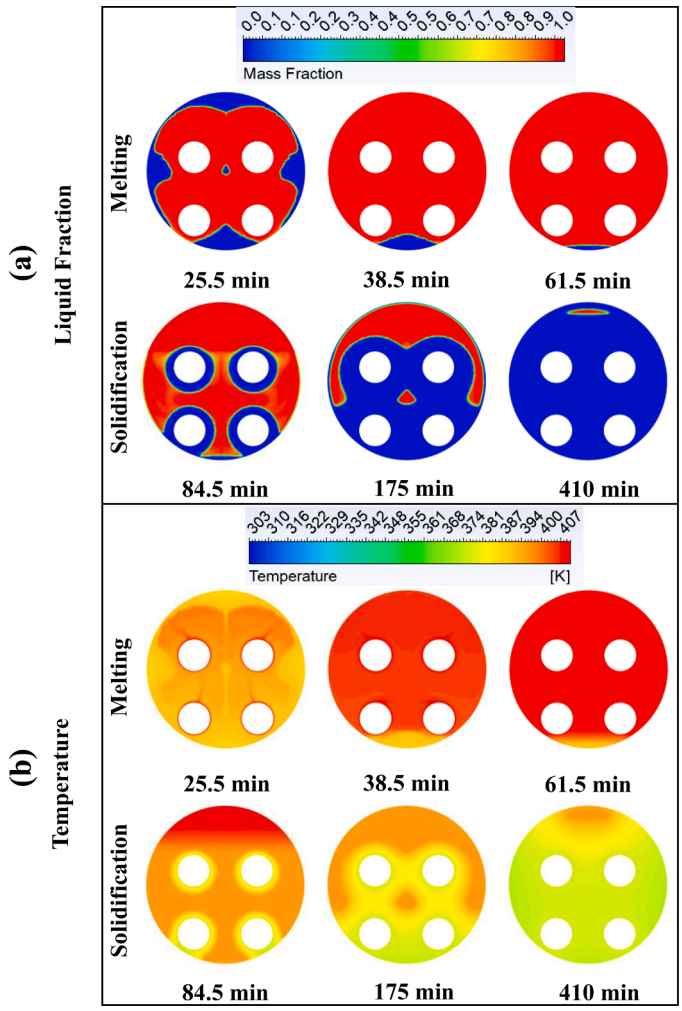

Fig. 17. Evolution of (a) liquid fraction and (b) temperature contours during melting and solidification processes for four-tube *'Eccentric Tubes/Circular Shell'* case.

the shrinking solid PCM. The overheated liquid PCM is seen when compared to temperature contours in Fig. 17b. 38.5th minute contour shows that the temperature of the melted PCM increases for PCM to completely melt. As depicted in the study of Gasia et al. [59]., temperature gradient at the end of the melting process subsequently affects the solidification of the PCM. Fig. 17b supports this idea and shows that the temperature of the PCM is greater at the top region.

In addition, Fig. 17a shows that natural convection is effective only at the beginning of the discharging process. Solidification begins around the HTF tubes and solidified PCM thickness grows faster at the bottom regions of the HTF tube due to natural convection. However, the solidification process is mostly dominated by the conduction heat transfer mechanism. Since the HTF tubes are arranged eccentrically, solidification develops formerly at the bottom.

Fig. 18a shows that the melting process is identical except the time delay of 4.5 min for domain to melt completely. Solidification process requires comparatively long time as can be seen from Fig. 18a; however, the comparison of Figs. 17a and 18a uncovers that the solidification speed increases as the shell shape becomes rectangular, i.e. fully solidified at 410th and 357th minutes.

Effects of heat losses are observed in liquid fraction contours at 28.5th min, Fig. 18a. Even though PCM is almost fully melted at the top region, a small amount of solid PCM still exists around the sidewalls of the LHTES unit. In the rectangular shell design, the time duration for melted PCM exposed to overheating is lower than in the circular shell

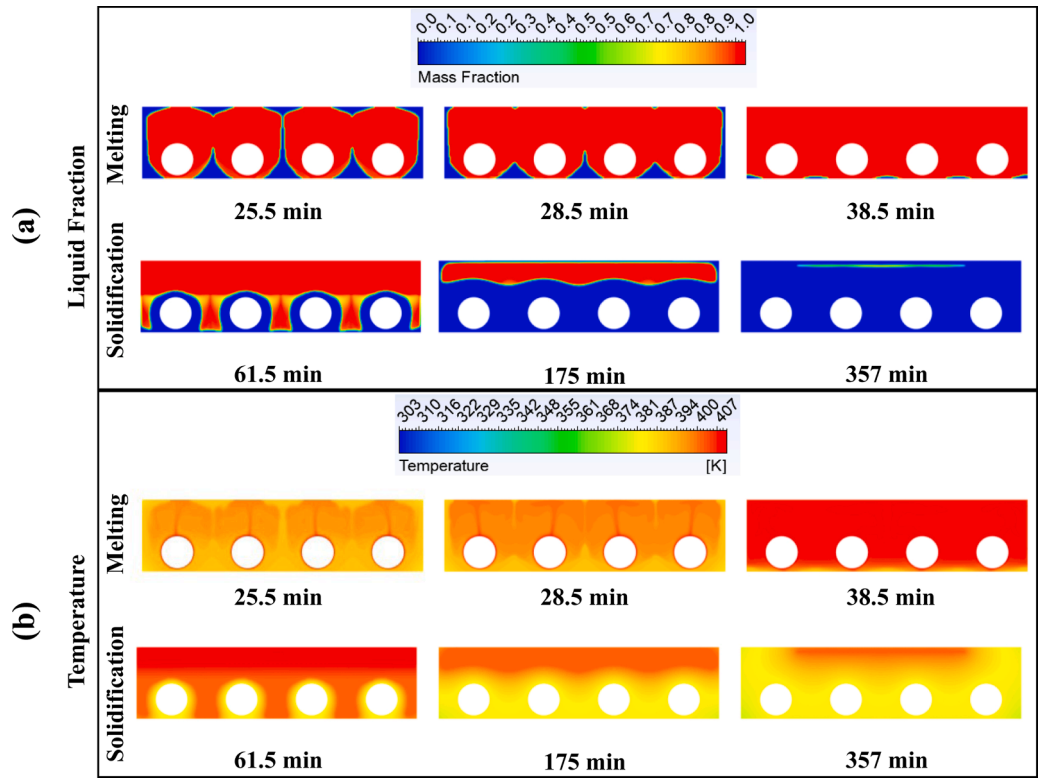

Fig. 18. Evolution of (a) liquid fraction and (b) temperature contours during melting and solidification processes for four-tube *'Eccentric Tubes/Rectangular Shell'* case.

design. PCM is completely melted at 39th min, and the solidification process starts. While the solidification process begins at 61.5th min in the circular shell design, it has already developed in the rectangular shell design at that time and the liquid fraction is 71.6%. However, Fig. 19a shows that liquid fractions of both designs become equal at 175th min because the temperature gradient is higher in the circular design at the end of the melting process, and solidification occurs rapidly. Nevertheless, the rectangular shell design completes the solidification process earlier as can be seen in Fig. 19a. In addition, Fig. 19b shows that the sensible enthalpy for circular shell design is greater than rectangular shell design during melting and solidification processes.

Table 2 shows that solidification time is much longer relative to melting time for both designs. The rectangular shell design performs better relative to the circular shell during both melting and solidification processes. The time-saving is 39%, 9%, and 13% in terms of melting, solidification, and total melting-solidification time, respectively.

Table 2
Storage performance of circular and rectangular shell designs.

Time(min) Designs	Melting	Solidification	Total
Eccentric Tubes/Circular Shell	61.5	349.5	411
Eccentric Tubes/Rectangular Shell	38	319	357
Time-Saving	39%	9%	13%

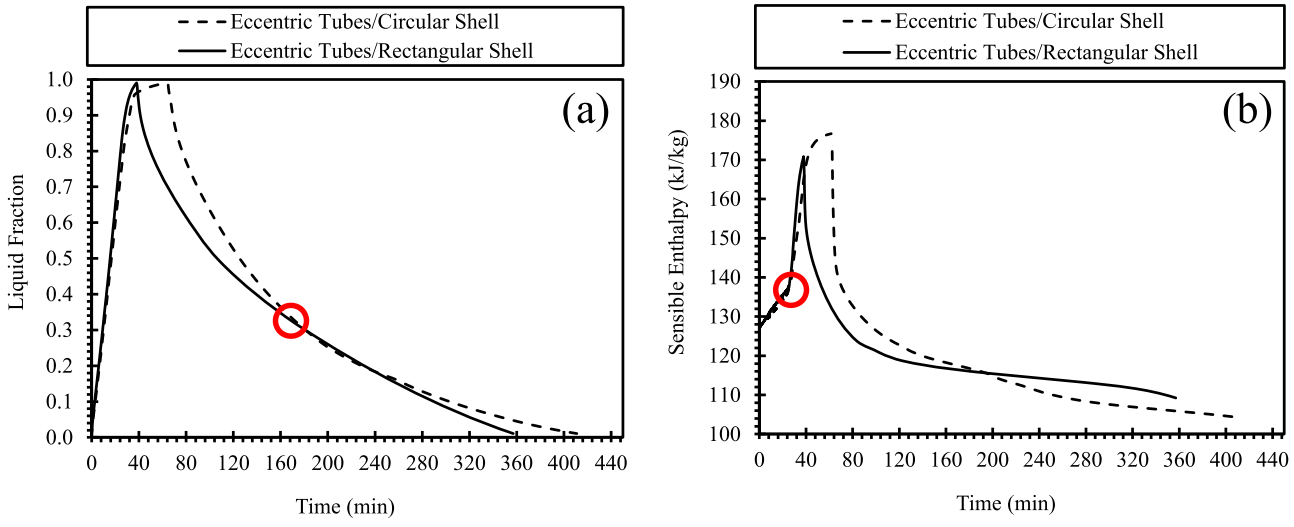

Fig. 19. Comparison of four-tube *'Eccentric Tubes/Circular Shell'* and *'Eccentric Tubes/Rectangular Shell'* cases for (a) liquid fraction and (b) sensible enthalpy.

Circular shells are conventionally preferred because heat loss to the environment is less relative to the rectangular shell. Here, the insulation material volume is fixed for circular and rectangular shell cases, i.e. insulation thicknesses correspond to 100 mm and 39 mm for the circular and rectangular shell designs, respectively.

Fig. 20a shows the variation of heat transfer rate at the walls of shells during melting and solidification. The heat transfer rate increases gradually during the melting process, and it reaches to the peak at the end of the melting processes for both shell designs. Then, it decreases during solidification until the time that PCM is in the fully solid-phase. According to Fig. 20a, heat transfer rate in the rectangular shell is greater than the circular shell design. The first reason is that the heat transfer surface area is greater in the rectangular shell design. The second is that the heat transfer resistance is lower due to the lower insulation thickness applied in the rectangular shell design because the volume of insulation material is fixed. Besides, increment in the sensible heat during the melting of PCM near the shell surface would increase the rate of heat transfer to the ambient. On the other side, total heat loss energy differs during the melting and solidification processes than the rate characteristics. The total heat loss energy in the rectangular shell design is lower than the circular shell during the melting process, as seen in Fig. 20b. That is because rectangular shell design completes the melting process 39% faster than the circular shell design. However, during the solidification process, the solidification time for the rectangular shell design is only 9% shorter than the circular shell design, and it cannot compensate for the disadvantage of low insulation resistance in the rectangular shell design. Therefore, the total heat loss energy is greater in the rectangular shell design. This increment in the total heat loss energy yields PCM to solidify faster in rectangular shell in comparison to the circular shell. Insulation thickness can be increased to reduce heat losses for the rectangular shell. However, it would increase the required time for solidification process. Moreover, as proposed in the study of Gasia et al. [59]. (experiments in the LHTES unit with a rectangular shell), partial melting and solidification can be applied for both melting and solidification processes since solid PCM would act as an insulation material at near shell boundary.

9. Conclusions

Here it was documented that how HTF tubes should be located and what should be the shape of shell tube to enhance melting time of PCM by natural convection and decrease the required sensible enthalpy for the process. First, a base design that has two tubes located in a circular shell was simulated. The results are in agreement with the literature, and they show that melting of PCM located below the tubes requires most of the melting time and increases sensible enthalpy greatly. Therefore, it was decided to pack melted regions in a fashion where they just touch each other when the solid completely melt to decrease melting time. Note that the volumes of PCM and tubes were fixed; therefore, the material originally located below the tubes were placed around the tubes. The improved design was selected to be rectangular due to: (1) a flat-edged bottom surface of the shell to be more applicable for eccentricity of multiple tubes, (2) similarity of melting front growth to a rectangular pack rather than the circular one, and (3) simplicity to manufacture. The alterations in tube spacing, eccentricity of the HTF tubes, and shell shape have led to the enhancement of melting due to increment in heat transfer rate via natural convection. Results show that when the shell design changes from circular to rectangular for two-tube cases, melting performance increases%38 within the time margin that the improved rectangular design reaches a fully-melted condition. Then, the effect of tube location and shell design was uncovered for four tubes. Results show that in order to minimize melting time, tubes should be located near the bottom end of the shell and the shell should be rectangular. Overall, the paper shows melting time and sensible heat storage can be decreased by just altering the design of the shell and positions of the tubes. For four-tube cases, the melting time decreased by 70% by applying eccentricity to the multi tubes. Changing shell shape from circular to rectangular with the eccentricity of multi tubes resulted in a 35% shorter melting time.

Literature documents that heat loss in rectangular shell shapes increases due to increment in heat transfer surface area. This is true in heat transfer rate definition. However, since the melting time in the rectangular shell design is 39% lower than the circular shell, the total heat loss energy becomes lower in the rectangular shell design during the melting process. During the solidification process, the total heat loss energy in the rectangular shell design is greater than the circular shell design because of the lower insulation thickness applied to keep the total insulation material constant for both circular and rectangular designs. Design improvements decreased not only melting time but also solidification time. Increasing the insulation thickness for rectangular shell or applying partial melting and solidification, it is possible to decrease the heat loss energy. Overall, this paper documents the optimal locations of tubes and shell shape can be decided by packing melted regions around the tubes which do not require an exhaustive search to minimize the heat loss energy for melting and the time required for melting and solidification for the applications with charging speed is a lot greater than the discharging speed.

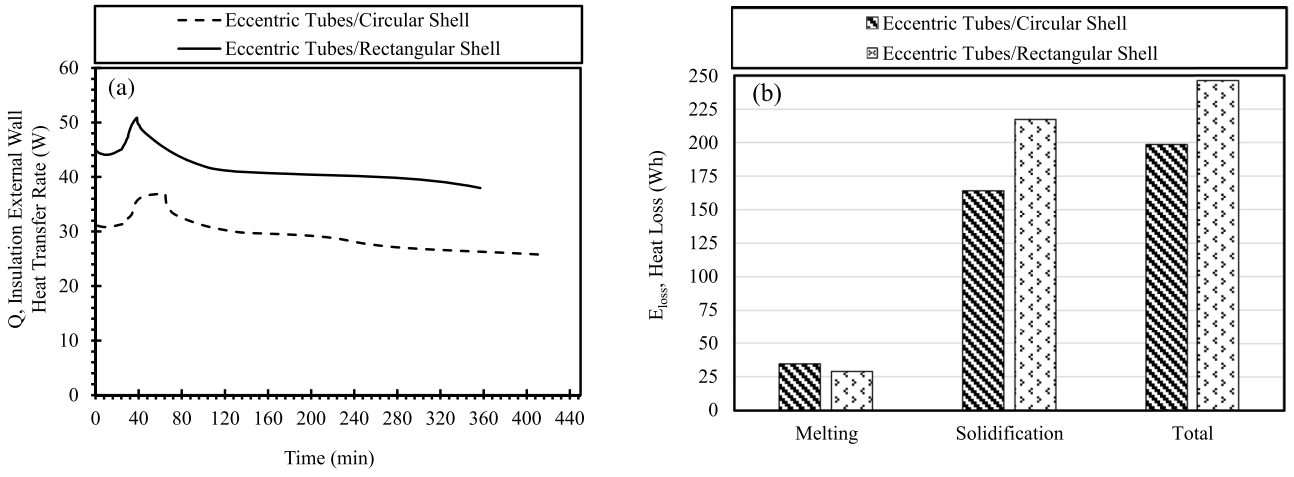

Fig. 20. (a) Evolution of heat transfer rate at insulation external wall during melting and solidification processes and (b) heat loss energy graph for four-tube *'Eccentric Tubes/Circular Shell'* and *'Eccentric Tubes/Rectangular Shell'* cases.

CRediT authorship contribution statement

İsmail Gürkan Demirkıran: Conceptualization, Methodology, Validation, Formal analysis, Visualization, Writing - original draft. **Erdal Cetkin:** Supervision, Conceptualization, Methodology, Writing - review & editing.

Declaration of Competing Interest

Dear Journal of Energy Storage Editors,

The authors whose names are listed immediately below certify that they have no affiliations with or involvement in any organization or entity with any financial interest (such as honoraria; educational grants; participation in speakers' bureaus; membership, employment, consultancies, stock ownership, or other equity interest; and expert testimony or patent-licensing arrangements), or non-financial interest (such as personal or professional relationships, affiliations, knowledge or beliefs) in the subject matter or materials discussed in the submitted manuscript entitled as "Emergence of rectangular shell shape in thermal energy storage applications: fitting melted PCM regions in a fixed space".

References

[1] Heat – Renewables 2019 – Analysis - IEA, (n.d.). https://www.iea.org/reports/renewables-2019/heat#abstract (accessed May 26, 2020).

[2] IRENA International Renewable Energy Agency, Renewable power generation costs in 2017, 2018. https://doi.org/10.1007/SpringerReference_7300.

[3] T. Okazaki, Y. Shirai, T. Nakamura, Concept study of wind power utilizing direct thermal energy conversion and thermal energy storage, Renew. Energy. 83 (2015) 332–338, https://doi.org/10.1016/j.renene.2015.04.027.

[4] M. Ciani Bassetti, D. Consoli, G. Manente, A. Lazzaretto, Design and off-design models of a hybrid geothermal-solar power plant enhanced by a thermal storage, Renew. Energy 128 (2018) 460–472, https://doi.org/10.1016/j.renene.2017.05.078.

[5] J.D. Templeton, F. Hassani, S.A. Ghoreishi-Madiseh, Study of effective solar energy storage using a double pipe geothermal heat exchanger, Renew. Energy 86 (2016) 173–181, https://doi.org/10.1016/j.renene.2015.08.024.

[6] S. Sharma, A. Tahir, K.S. Reddy, T.K. Mallick, Performance enhancement of a building-integrated concentrating photovoltaic system using phase change material, Sol. Energy Mater. Sol. Cells. 149 (2016) 29–39, https://doi.org/10.1016/j.solmat.2015.12.035.

[7] U.N. Temel, Passive thermal management of a simulated battery pack at different climate conditions, Appl. Therm. Eng. 158 (2019), 113796, https://doi.org/10.1016/j.applthermaleng.2019.113796.

[8] K. Merlin, J. Soto, D. Delaunay, L. Traonvouez, Industrial waste heat recovery using an enhanced conductivity latent heat thermal energy storage, Appl. Energy. 183 (2016) 491–503, https://doi.org/10.1016/j.apenergy.2016.09.007.

[9] M. Alam, P.X.W. Zou, J. Sanjayan, S. Ramakrishnan, Energy saving performance assessment and lessons learned from the operation of an active phase change materials system in a multi-storey building in Melbourne, Appl. Energy 238 (2019) 1582–1595, https://doi.org/10.1016/j.apenergy.2019.01.116.

[10] J.C. Kurnia, A.P. Sasmito, Numerical investigation of heat transfer performance of a rotating latent heat thermal energy storage, Appl. Energy 227 (2018) 542–554, https://doi.org/10.1016/j.apenergy.2017.08.087.

[11] N. Zhang, Y. Du, Ultrasonic enhancement on heat transfer of palmitic-stearic acid as PCM in unit by experimental study, Sustain. Cities Soc. 43 (2018) 532–537, https://doi.org/10.1016/j.scs.2018.08.040.

[12] M. Esapour, A. Hamzehnezhad, A.A. Rabienataj Darzi, M. Jourabian, Melting and solidification of PCM embedded in porous metal foam in horizontal multi-tube heat storage system, Energy Convers. Manag. 171 (2018) 398–410, https://doi.org/10.1016/j.enconman.2018.05.086.

[13] Z. Liu, Y. Yao, H. Wu, Numerical modeling for solid-liquid phase change phenomena in porous media: shell-and-tube type latent heat thermal energy storage, Appl. Energy. 112 (2013) 1222–1232, https://doi.org/10.1016/j.apenergy.2013.02.022.

[14] C.Y. Zhao, Z.G. Wu, Heat transfer enhancement of high temperature thermal energy storage using metal foams and expanded graphite, Sol. Energy Mater. Sol. Cells. 95 (2011) 636–643, https://doi.org/10.1016/j.solmat.2010.09.032.

[15] L. Qiu, Y. Ouyang, Y. Feng, X. Zhang, Review on micro/nano phase change materials for solar thermal applications, Renew. Energy 140 (2019) 513–538, https://doi.org/10.1016/j.renene.2019.03.088.

[16] H.C. Konan, E. Cetkin, Snowflake shaped high-conductivity inserts for heat transfer enhancement, Int. J. Heat Mass Transf. 127 (2018) 473–482, https://doi.org/10.1016/j.ijheatmasstransfer.2018.08.063.

[17] A. Pizzolato, A. Sharma, K. Maute, A. Sciacovelli, V. Verda, Design of effective fins for fast PCM melting and solidification in shell-and-tube latent heat thermal energy storage through topology optimization, Appl. Energy. 208 (2017) 210–227, https://doi.org/10.1016/j.apenergy.2017.10.050.

[18] A.M. Abdulateef, J. Abdulateef, S. Mat, K. Sopian, B. Elhub, M.A. Mussa, Experimental and numerical study of solidifying phase-change material in a triplex-tube heat exchanger with longitudinal/triangular fins, Int. Commun. Heat Mass Transf. 90 (2018) 73–84, https://doi.org/10.1016/j.icheatmasstransfer.2017.10.003.

[19] A.M. Abdulateef, S. Mat, J. Abdulateef, K. Sopian, A.A. Al-Abidi, Geometric and design parameters of fins employed for enhancing thermal energy storage systems: a review, Renew. Sustain. Energy Rev. 82 (2018) 1620–1635, https://doi.org/10.1016/j.rser.2017.07.009.

[20] F. Agyenim, P. Eames, M. Smyth, Heat transfer enhancement in medium temperature thermal energy storage system using a multitube heat transfer array, Renew. Energy 35 (2010) 198–207, https://doi.org/10.1016/j.renene.2009.03.010.

[21] N. Kousha, M. Rahimi, R. Pakrouh, R. Bahrampoury, Experimental investigation of phase change in a multitube heat exchanger, J. Energy Storage 23 (2019) 292–304, https://doi.org/10.1016/j.est.2019.03.024.

[22] M. Esapour, M.J. Hosseini, A.A. Ranjbar, Y. Pahamli, R. Bahrampoury, Phase change in multi-tube heat exchangers, Renew. Energy 85 (2016) 1017–1025, https://doi.org/10.1016/j.renene.2015.07.063.

[23] A.J. Parry, P.C. Eames, F.B. Agyenim, Modeling of thermal energy storage shell-and-tube heat exchanger, Heat Transf. Eng. 35 (2014) 1–14, https://doi.org/10.1080/01457632.2013.810057.

[24] K. Luo, F.J. Yao, H.L. Yi, H.P. Tan, Lattice Boltzmann simulation of convection melting in complex heat storage systems filled with phase change materials, Appl. Therm. Eng. 86 (2015) 238–250, https://doi.org/10.1016/j.applthermaleng.2015.04.059.

[25] R. Dutta, A. Atta, T.K. Dutta, Experimental and numerical study of heat transfer in horizontal concentric annulus containing phase change material, Can. J. Chem. Eng. 86 (2008) 700–710, https://doi.org/10.1002/cjce.20075.

[26] Y. Pahamli, M.J. Hosseini, A.A. Ranjbar, R. Bahrampoury, Analysis of the effect of eccentricity and operational parameters in PCM-filled single-pass shell and tube heat exchangers, Renew. Energy 97 (2016) 344–357, https://doi.org/10.1016/j.renene.2016.05.090.

[27] A.A.R. Darzi, M. Farhadi, K. Sedighi, Numerical study of melting inside concentric and eccentric horizontal annulus, Appl. Math. Model. 36 (2012) 4080–4086, https://doi.org/10.1016/j.apm.2011.11.033.

[28] X. Cao, Y. Yuan, B. Xiang, F. Highlight, Effect of natural convection on melting performance of eccentric horizontal shell and tube latent heat storage unit, Sustain. Cities Soc. 38 (2018) 571–581, https://doi.org/10.1016/j.scs.2018.01.025.

[29] M.Y. Yazici, M. Avci, O. Aydin, M. Akgun, On the effect of eccentricity of a horizontal tube-in-shell storage unit on solidification of a PCM, Appl. Therm. Eng. 64 (2014) 1–9, https://doi.org/10.1016/j.applthermaleng.2013.12.005.

[30] Z.J. Zheng, Y. Xu, M.J. Li, Eccentricity optimization of a horizontal shell-and-tube latent-heat thermal energy storage unit based on melting and melting-solidifying performance, Appl. Energy 220 (2018) 447–454, https://doi.org/10.1016/j.apenergy.2018.03.126.

[31] M.R. Kadivar, M.A. Moghimi, P. Sapin, C.N. Markides, Annulus eccentricity optimisation of a phase-change material (PCM) horizontal double-pipe thermal energy store, J. Energy Storage 26 (2019), 101030, https://doi.org/10.1016/j.est.2019.101030.

[32] Y. Xu, Z.J. Zheng, S. Chen, X. Cai, C. Yang, Parameter analysis and fast prediction of the optimum eccentricity for a latent heat thermal energy storage unit with phase change material enhanced by porous medium, Appl. Therm. Eng. 186 (2021), 116485, https://doi.org/10.1016/j.applthermaleng.2020.116485.

[33] N.S. Dhaidan, J.M. Khodadadi, T.A. Al-Hattab, S.M. Al-Mashat, Experimental and numerical investigation of melting of NePCM inside an annular container under a constant heat flux including the effect of eccentricity, Int. J. Heat Mass Transf. 67 (2013) 455–468, https://doi.org/10.1016/j.ijheatmasstransfer.2013.08.002.

[34] R. Kumar, P. Verma, An experimental and numerical study on effect of longitudinal finned tube eccentric configuration on melting behaviour of lauric acid in a horizontal tube-in-shell storage unit, J. Energy Storage 30 (2020), 101396, https://doi.org/10.1016/j.est.2020.101396.

[35] M. Faghani, M.J. Hosseini, R. Bahrampoury, Numerical simulation of melting between two elliptical cylinders, Alexandria Eng. J. 57 (2018) 577–586, https://doi.org/10.1016/j.aej.2017.02.003.

[36] J. Vogel, J. Felbinger, M. Johnson, Natural convection in high temperature flat plate latent heat thermal energy storage systems, Appl. Energy. 184 (2016) 184–196, https://doi.org/10.1016/j.apenergy.2016.10.001.

[37] S. Seddegh, X. Wang, A.D. Henderson, A comparative study of thermal behaviour of a horizontal and vertical shell-and-tube energy storage using phase change materials, Appl. Therm. Eng. 93 (2016) 348–358, https://doi.org/10.1016/j.applthermaleng.2015.09.107.

[38] F. Agyenim, The use of enhanced heat transfer phase change materials (PCM) to improve the coefficient of performance (COP) of solar powered LiBr/H2O absorption cooling systems, Renew. Energy 87 (2016) 229–239, https://doi.org/10.1016/j.renene.2015.10.012.

[39] B. Li, X. Zhai, X. Cheng, Experimental and numerical investigation of a solar collector/storage system with composite phase change materials, Sol. Energy 164 (2018) 65–76, https://doi.org/10.1016/j.solener.2018.02.031.

[40] A. Papadimitratos, S. Sobhansarbandi, V. Pozdin, A. Zakhidov, F. Hassanipour, Evacuated tube solar collectors integrated with phase change materials, Sol. Energy. 129 (2016) 10–19, https://doi.org/10.1016/j.solener.2015.12.040.

[41] B. Li, X. Zhai, Experimental investigation and theoretical analysis on a mid-temperature solar collector/storage system with composite PCM, Appl. Therm. Eng. 124 (2017) 34–43, https://doi.org/10.1016/j.applthermaleng.2017.06.002.

[42] M.A. Essa, N.H. Mostafa, M.M. Ibrahim, An experimental investigation of the phase change process effects on the system performance for the evacuated tube solar collectors integrated with PCMs, Energy Convers. Manag. 177 (2018) 1–10, https://doi.org/10.1016/j.enconman.2018.09.045.
[43] R. Senthil, P. Sundaram, Improvement of thermal energy storage density of parabolic dish solar absorber with organic phase change materials, IOP Conf. Ser. Mater. Sci. Eng. (2018) 402, https://doi.org/10.1088/1757-899X/402/1/012046.
[44] A. Mawire, T.M. Lefenya, C.S. Ekwomadu, K.A. Lentswe, A.B. Shobo, Performance comparison of medium temperature domestic packed bed latent heat storage systems, Renew. Energy 146 (2020) 1897–1906, https://doi.org/10.1016/j.renene.2019.08.063.
[45] A. Kaizawa, H. Kamano, A. Kawai, T. Jozuka, T. Senda, N. Maruoka, T. Akiyama, Thermal and flow behaviors in heat transportation container using phase change material, Energy Convers. Manag. 49 (2008) 698–706, https://doi.org/10.1016/j.enconman.2007.07.022.
[46] J.N.W. Chiu, Industrial surplus heat storage in smart cities, (2016) 1–8.
[47] F. Agyenim, N. Hewitt, P. Eames, M. Smyth, A review of materials, heat transfer and phase change problem formulation for latent heat thermal energy storage systems (LHTESS), Renew. Sustain. Energy Rev. 14 (2010) 615–628, https://doi.org/10.1016/j.rser.2009.10.015.
[48] Y. Wang, L. Wang, N. Xie, X. Lin, H. Chen, Experimental study on the melting and solidification behavior of erythritol in a vertical shell-and-tube latent heat thermal storage unit, Int. J. Heat Mass Transf. 99 (2016) 770–781, https://doi.org/10.1016/j.ijheatmasstransfer.2016.03.125.
[49] V.R. Voller, C. Prakash, A fixed grid numerical modelling methodology for convection-diffusion mushy region phase-change problems, Int. J. Heat Mass Transf. 30 (1987) 1709–1719, https://doi.org/10.1016/0017-9310(87)90317-6.
[50] ANSYS Fluent Software | CFD Simulation, ANSYS, Inc. (2019). https://www.ansys.com/products/fluids/ansys-fluent (accessed October 15, 2019).
[51] F. Agyenim, P. Eames, M. Smyth, A comparison of heat transfer enhancement in a medium temperature thermal energy storage heat exchanger using fins, Sol. Energy. 83 (2009) 1509–1520, https://doi.org/10.1016/j.solener.2009.04.007.
[52] N.S. Dhaidan, J.M. Khodadadi, Melting and convection of phase change materials in different shape containers: a review, Renew. Sustain. Energy Rev. 43 (2015) 449–477, https://doi.org/10.1016/j.rser.2014.11.017.
[53] Y.B. Tao, Y.L. He, Effects of natural convection on latent heat storage performance of salt in a horizontal concentric tube, Appl. Energy (2015), https://doi.org/10.1016/j.apenergy.2015.01.008.
[54] J. Vogel, M. Johnson, Natural convection during melting in vertical finned tube latent thermal energy storage systems, Appl. Energy. 246 (2019) 38–52, https://doi.org/10.1016/j.apenergy.2019.04.011.
[55] D. Yanxia, Y. Yanping, J. Daiyong, C. Baoyi, M. Jinfeng, Experimental investigation on melting characteristics of ethanolamine-water binary mixture used as PCM, Int. Commun. Heat Mass Transf. 34 (2007) 1056–1063, https://doi.org/10.1016/j.icheatmasstransfer.2007.07.002.
[56] M. Esapour, M.J. Hosseini, A.A. Ranjbar, R. Bahrampoury, Numerical study on geometrical specifications and operational parameters of multi-tube heat storage systems, Appl. Therm. Eng. 109 (2016) 351–363, https://doi.org/10.1016/j.applthermaleng.2016.08.083.
[57] S. Lakhani, A. Raul, S.K. Saha, Dynamic modelling of ORC-based solar thermal power plant integrated with multitube shell and tube latent heat thermal storage system, Appl. Therm. Eng. 123 (2017) 458–470, https://doi.org/10.1016/j.applthermaleng.2017.05.115.
[58] E. Cetkin, S. Lorente, A. Bejan, The steepest S curve of spreading and collecting flows: discovering the invading tree, not assuming it, J. Appl. Phys. (2012) 111, https://doi.org/10.1063/1.4721657.
[59] J. Gasia, A. de Gracia, G. Zsembinszki, L.F. Cabeza, Influence of the storage period between charge and discharge in a latent heat thermal energy storage system working under partial load operating conditions, Appl. Energy. 235 (2019) 1389–1399, https://doi.org/10.1016/j.apenergy.2018.11.041.